Research paper

The late Eocene rise of SE Tibet formed an Asian 'Mediterranean' climate

Chenyuan Zhao [a,b,1], Zhongyu Xiong [a,*,1], Alex Farnsworth [a,d], Robert A. Spicer [a,c,e], Songlin He [a], Chao Wang [a], Deng Zeng [a,b], Fulong Cai [a,b], Houqi Wang [a], Xiaolong Tian [a,b], Paul J. Valdes [d], Ciren Lamu [a,b], Jing Xie [a], Yahui Yue [a], Lin Ding [a,b,*]

[a] State Key Laboratory of Tibetan Plateau Earth System, Environment and Resources, Institute of Tibetan Plateau Research, Chinese Academy of Sciences, Beijing 100101, China
[b] University of Chinese Academy of Sciences, Beijing 100049, China
[c] School of Environment, Earth and Ecosystem Sciences, the Open University, Milton Keynes MK7 6AA, UK
[d] School of Geographical Sciences, University of Bristol, Bristol BS8 1SS, UK
[e] Xishuangbanna Tropical Botanical Garden, Chinese Academy of Sciences, Mengla 666303, China

ARTICLE INFO

ABSTRACT

Southeastern (SE) Tibet forms the transition zone between the high interior Tibetan Plateau and the lowlands of southwest China. So understanding the elevation history of SE Tibet, a biodiversity hotspot, enlightens our understanding of the interactions between tectonics, monsoon dynamics and biodiversity. Here we reconstruct the uplift history of the Markam Basin, SE Tibet, during the middle−late Eocene based on U − Pb dating, plant fossil assemblages, and stable and clumped isotope analyses. Our results suggest that the floor of the Markam Basin was at an elevation of 2.6 ± 0.9 km between 42 Ma and 39 Ma, where the mean annual air temperature (MAAT) was 13.2 ± 2.4 °C. The basin then rose rapidly to 3.8 (+0.6/−0.8) km before 36 Ma. Integrated with existing paleoelevation data, we propose that the high plateau boundary (~3.0 km) of SE Tibet formed during the late Eocene. Numerical climate modeling with realistic paleo-landscapes shows that with the rise of SE Tibet, a Mediterranean-like climate developed in the region characterized by bi-modal precipitation with two wet seasons in boreal spring and autumn. The high topographic relief of SE Tibet, coupled with this distinctive Mediterranean-like climate system, helped develop the high biodiversity of the Hengduan Mountains.

1. Introduction

As the world's largest and highest elevated area, the Tibetan-Himalaya-Hengduan Mountains (THH) Region is the most distinctive topographic feature on Earth. The rise of the THH played a significant role in Asian climate and drainage evolution, potentially driving floral and faunal diversity (Ding et al., 2020; Molnar et al., 2010; Yao et al., 2015).

Southeastern (SE) Tibet now comprises the high relief Hengduan Mountains, which seem to have undergone intense Miocene dissection of a long-wavelength, low-gradient ramp-like topography (Cao et al., 2019; Liu et al., 2022). Today it forms the transitional area where the South Asian Monsoon and East Asian Monsoon systems interact. The complex topography, coupled with a wet monsoonal climate, makes SE Tibet one of the global biodiversity hotspots (Antonelli et al., 2018).

However, the timing and mechanism of the topographic evolution of SE Tibet, their impact on the evolution of the Asian monsoon system, and the regional diversification of species, are still unclear (He et al., 2022; Sarr et al., 2022).

Lower crustal flow used to be a widely accepted explanation for the smooth topographic gradients of SE Tibet (Clark and Royden, 2000; Royden et al., 1997). The evidence supporting this hypothesis was based on numerical modeling of ductile flow in the lower crust (Clark and Royden, 2000; Clark et al., 2005). Early analysis of river capture along the major rivers and their tributaries flowing from SE Tibet (Clark et al., 2004) and thermochronological data as well as cosmogenic nuclide erosion rates revealed a rapid Miocene−Pliocene cooling episode (Clark et al., 2005, 2006). This was interpreted as a Miocene rise of SE Tibet driven by lower crustal flow. However, recent evidence from quantitative paleoaltimetry, thermochronology and provenance analyses

suggested major uplift of SE Tibet occurred in Eocene−Oligocene time (Cao et al., 2019; He et al., 2022; Hoke et al., 2014; Su et al., 2019; Tao et al., 2022; Xiong et al., 2020). The Miocene rapid cooling episode was further interpreted as being caused by either the intensification of the South Asian monsoon or the progressive indentation of India and

corresponding deformation, increasing erosion rates along the major rivers (Chen et al., 2021; Nie et al., 2018; Yang et al., 2016).

The onset of the Asian monsoon has long been linked to the development of the THH and/or the retreat of the Paratethys (Molnar et al., 1993, 2010; Ramstein et al., 1997). Recently, orbital variability, pCO_2,
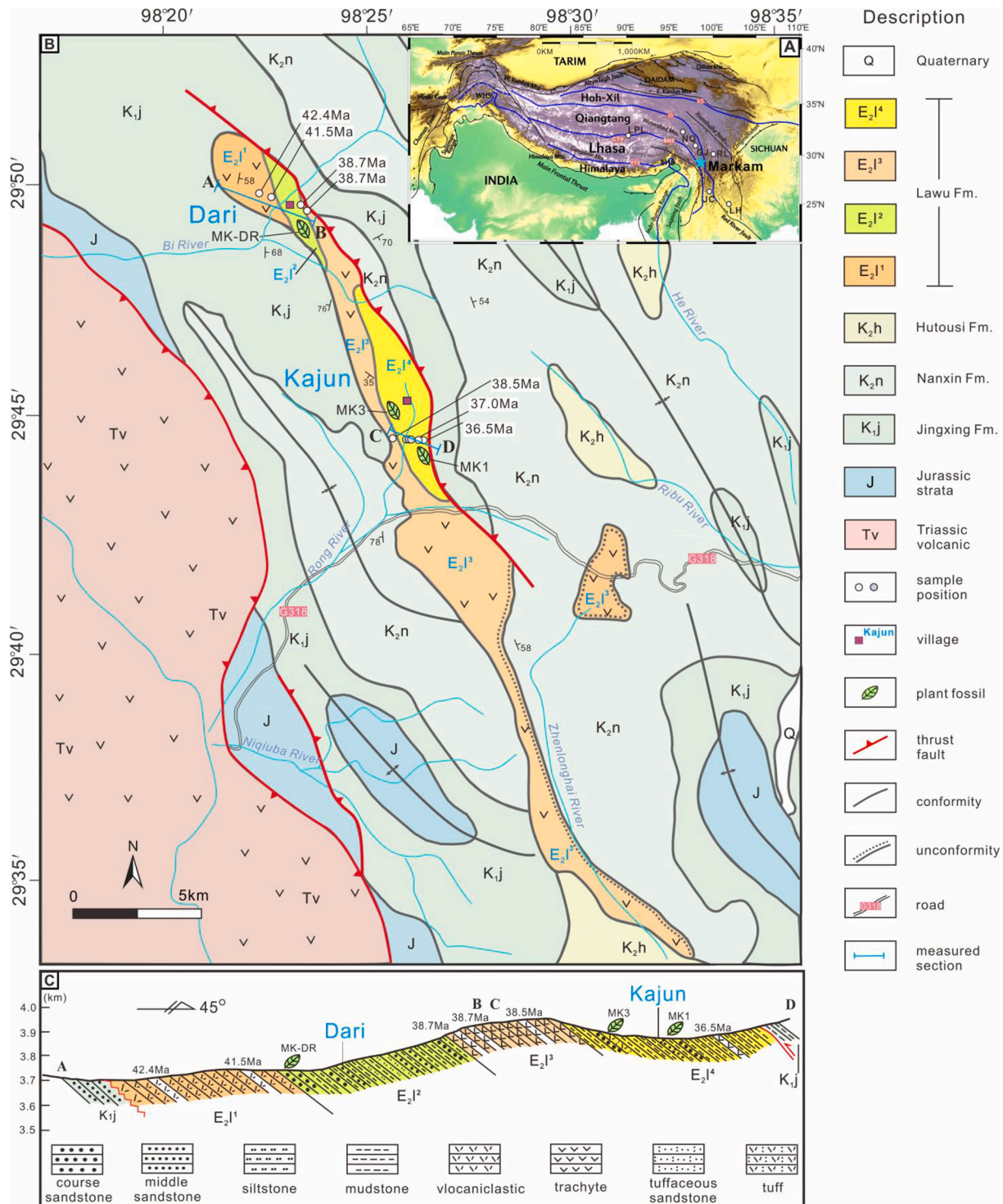

Fig. 1. Tectonic context and geological background of the Markam Basin.A. Tectonic terranes and sutures of the Tibetan Plateau. From south to north, major terranes are the Himalaya terrane, the Lhasa terrane, the Qiangtang terrane and the Hoh-Xil terrane.B. Geologic map of the Markam Basin with measured sections and sampled positions. The white circles are volcanic samples, and gray circles are carbonate samples. C. Composite geological cross-section A − B and C − D showing the main structures and strata of the Markam Basin with corresponding lithology, age constraints and representative floras. Abbreviations: KS, Kunlun suture; JS, Jinshajiang suture; BNS, Bangong-Nujiang suture; YTS, Yarlung-Tsangpo suture; CTV, Central Tibet Valley; WHS: west Himalaya syntaxis; EHS: east Himalaya syntaxis; NQ, Nangqian Basin; GJ, Gonjo Basin; RL, Relu Basin; JC, Jianchuan Basin; LH, Lühe Basin; LPL, Lunpola Basin. Fig. 1A was based on Ding et al. (2022).

ice-sheet state and ocean gateways have also been invoked as contributing to the development of South Asian Monsoon, while paleogeography is the dominant controlling factor on the East Asian monsoon (Farnsworth et al., 2019; Tardif et al., 2020; Thomson et al., 2021). However, the timing of the onset of the Asian monsoon varies from late Cretaceous to Early Miocene (Fang et al., 2020; Farnsworth et al., 2019; Guo et al., 2008; He et al., 2022; Licht et al., 2014). Besides timing, the coupling process between differential topographic change of the THH and development of the Asian monsoon remains to be further explored (Fang et al., 2020; Spicer et al., 2017, 2021). The pervasive distribution of Cretaceous−early Paleogene "red beds" from SE Tibet to eastern China indicates an arid to semi-arid climate existing before the Cenozoic amplification of the Asian monsoon climate (He et al., 2022; Jiang et al., 2012; Zheng et al., 2022). With the rise of SE Tibet and the transformation from an arid to a distinctive monsoonal climate during the Paleogene, the elevational gradient and climatic diversity in this region provided a wide range of ecological niches for species evolution (Hoorn et al., 2018) and cultivated the initial biodiversity 'hotspot' within the Hengduan Mountains (He et al., 2022; Tian et al., 2021).

Within the context of field mapping and sampling, we constructed a U − Pb geochronology, undertook numerical analysis of plant fossil assemblages, and together with oxygen and clumped isotope studies within the Markam Basin, SE Tibet, we established quantitatively the elevation history of the basin during the middle to late Eocene (mostly Bartonian, ca. 42–36 Ma). Integrated with a review of existing paleo-elevation and paleoclimate data, we document the formation of a high SE Tibet by the late Eocene. The elevated topography highlights the generation of a peculiar Eocene Mediterranean-like climate system across the region.

2. Geologic setting

SE Tibet forms a distinctive high topographic relief boundary of the THH uplands and comprises several continental fragments, including the Lhasa, Qiangtang, and Songpan-Ganzi terranes, the Yidun Arc, and the South China, Tengchong-Baoshan and Lanping-Simao terranes (Yin and Harrison, 2000). Three large rivers (the Salween, Mekong and Yangtze) flow nearly in parallel within SE Tibet from 31°N to 26°N and carve deep gorges with relief up to 3 km (Liu-Zeng et al., 2008). SE Tibet is also cut by large-scale strike-slip and thrust fault systems, specifically the Gaoligong, Ailaoshan-Red River and Xiaojiang faults (Wang et al., 1998). Together with the Nangqian-Yushu thrust belt, the Yalong and Longmen Shan thrust belts, strike-slip and thrust fault activities have controlled the complicated shortening, rotation and extrusion history of SE Tibet (Burchfiel and Chen, 2012; Horton et al., 2002). A series of Cenozoic basins including Nangqian, Gonjo, Markam and Relu basins co-evolved with the deformation.

The NW-SE-oriented Markam Basin, located in the eastern part of the Qiangtang Terrane and geographically in the northern part of Hengduan Mountains, comprises Cenozoic strata covering an area of 40 km^2 (Fig. 1A). The average altitude within the basin is ~4300 m. Today the climate in the Markam Basin is semi-humid monsoonal with a mean annual air temperature (MAAT) of 3.9 °C and annual precipitation of 590 mm/yr.

Pre-Cenozoic strata within the Markam Basin include Cretaceous terrestrial units known as the Jingxing (K_1j), Nanxin (K_2n) and Hutousi (K_2h) formations, which are thrusted over Triassic volcanics (Fig. 1B). In the western boundary of the basin, the Cenozoic Lawu Fm. (E_2l) unconformably overlies folded Cretaceous rocks, while in the eastern boundary, the E_2l is in fault contact with Cretaceous strata. The E_2l mainly consists of interbedded volcaniclastic rocks and lacustrine strata, with a small portion of fluvial and swamp deposits characterized by paleosol nodules and coal layers, respectively.

Two sections (Dari and Kajun) were measured and the generalized cross section is given (Fig. 1C) based on the field work. The total thickness of the Lawu Fm. is ~600 m and is divided into 4 units (Fig. 2 and 3). The first unit (E_2l^1) comprises two distinct lithological parts. The lower part is characterized by a succession of volcaniclastics >100-m-thick, but the clast compositions within these volcaniclastics are unclear due to petrogenic alteration (Fig. S1a, Fig. S1b). The upper part is a ~ 30-m-thick succession of volcaniclastics interbedded with yellow mudstone and siltstone layers (Fig. 2A). The second unit (E_2l^2) comprises ~130 m of yellow course- to medium- grained sandstones, as well as horizontally bedded siltstones and mudstones (Fig. 2B). The recurring cross-laminated coarse sandstone layers and bedded mudstone layers represent periodic changes in relative high energy and low energy conditions, indicating the water level fluctuated periodically and point to lakeshore facies. Abundant plant fossils are preserved in the lower bedded mudstone and are referred to as the MK-DR flora (Fig. 2C). The third unit (E_2l^3) is an ~100-m-thick trachyte, which is widely distributed within the entire basin (Fig. 2D). The fourth unit (E_2l^4) is an ~200-m-thick gray to yellow mudstone, interbedded with shale, medium grained sandstones and tuffaceous sandstone bands (Fig. 2E, G, H). Siderite-bearing nodules and calcite nodules are formed in the interbedded layers of siltstone and mudstone, and represent periodical drying that promoted the formation of oxygen-depleted paleosols and carbonate deposition. Thin coal horizons in the shale and parallel bedding represent relatively low energy depositional conditions and indicate high organic productivity around the lake margin or swamp (Fig. 2F).

3. Materials and methods

3.1. U − Pb Geochronology

Nine age samples were collected systematically comprising volcaniclastic rocks, trachyte, tuff and tuffaceous sandstones, from which zircons were selected for dating. All dating work was performed at the State Key Laboratory of Tibetan Plateau Earth System, Environment and Resources (TPESER), Institute of Tibetan Plateau Research, Chinese Academy of Sciences (ITPCAS). Zircon U − Pb dating was conducted using a New Wave UP 193FX Excimer laser (New Wave Instrument, USA) coupled to an Agilent 7500a inductively coupled plasma mass spectrometer (LA-ICP-MS). Depending on the zircon grain size, a beam spot diameter of 35 μm or 30 μm was used with an 8 Hz repetition rate and an energy of ~5–8 J/cm^2. Plešovice standard zircon (337 ± 0.37 Ma) (Sláma et al., 2008) and 91,500 standard zircon (1064 ± 4.0 Ma) (Wiedenbeck et al., 1995) were used to monitor and calibrate data from the raw samples. NIST SRM 610 standard glass was analyzed as an external standard for further trace element content calibration, with ^{29}Si as the internal standard element. Offline isotope ratios and trace element concentrations were calculated using Iolite V4. The common Pb correction was based on Andersen (2002). The U − Pb Concordia plots, age distribution frequency plots and weighted mean age plots were performed using the Isoplot program (Ludwig, 2003). The U − Pb isotope results were placed on the Wetherill-type Concordia diagram with 1σ error. All the U − Pb data are provided in Table S1.

3.2. Fossil materials and Climate Leaf Analysis Multivariate Program (CLAMP)

Plant fossils were collected from the E_2l^2 unit in Dari country (29°49′42.17″N, 98°23′26.61″E). After being cleaned and numbered, fossils were photographed under natural light with a Canon R5 camera. Morphological detail was observed and recorded using a macro-lens. A total of 48 dicotyledonous fossil leaf morphotypes were identified, and the representative fossils are showed in Fig. 5. Our numerical description and scoring of leaf physiognomic characteristics followed the protocols on the CLAMP website (http://clamp.ibcas.ac.cn). To decode the paleoclimate signal preserved in the MK-DR fossil leaf assemblages, the PhysgAsia2 physiognomic file paired with 1-km resolution gridded climate dataset−WorldClim2 was used to calibrate CLAMP (Fick and Hijmans, 2017). The scoring sheet and CLAMP results are available as
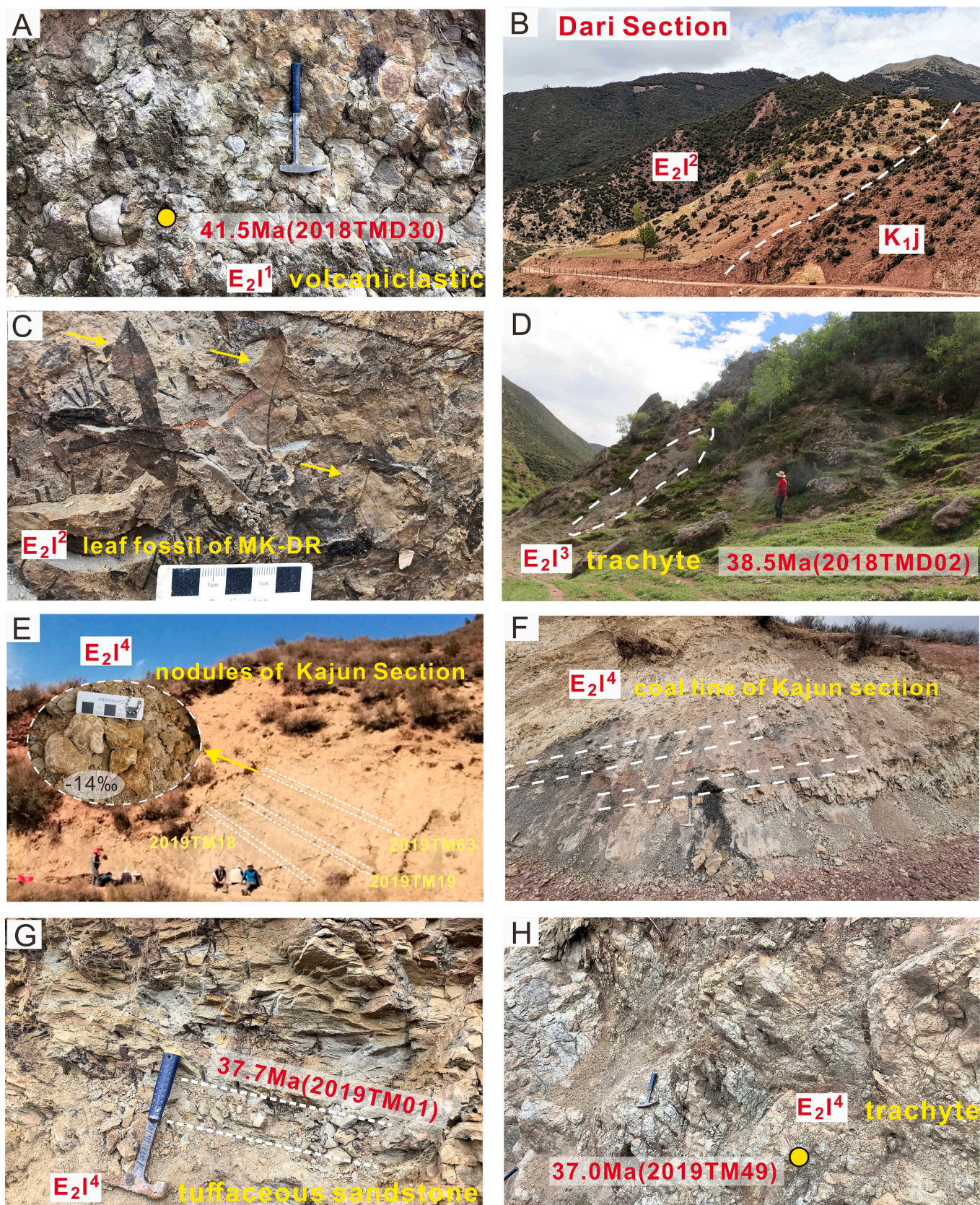
Fig. 2. Representative field photos in the Markam Basin. A. The volcaniclastic sample in the upper part of E_2l^1. B. The upper strata of the Dari section with yellow mudstone and sandstone thrusted over the Jingxing Fm. (K_1j). C. The sampled location of MK-DR flora in E_2l^2. D. Trachyte sample in E_2l^3. E. Nodule samples in E_2l^4 at the Kajun section. F. Coaly horizons in Kajun section. G. Layer of tuffaceous sandstone near the MK3 flora (2019TM01) in E_2l^4. H. Trachyte in E_2l^4 at the Kajun section (2019TM49). (For interpretation of the references to colour in this figure legend, the reader is referred to the web version of this article.)
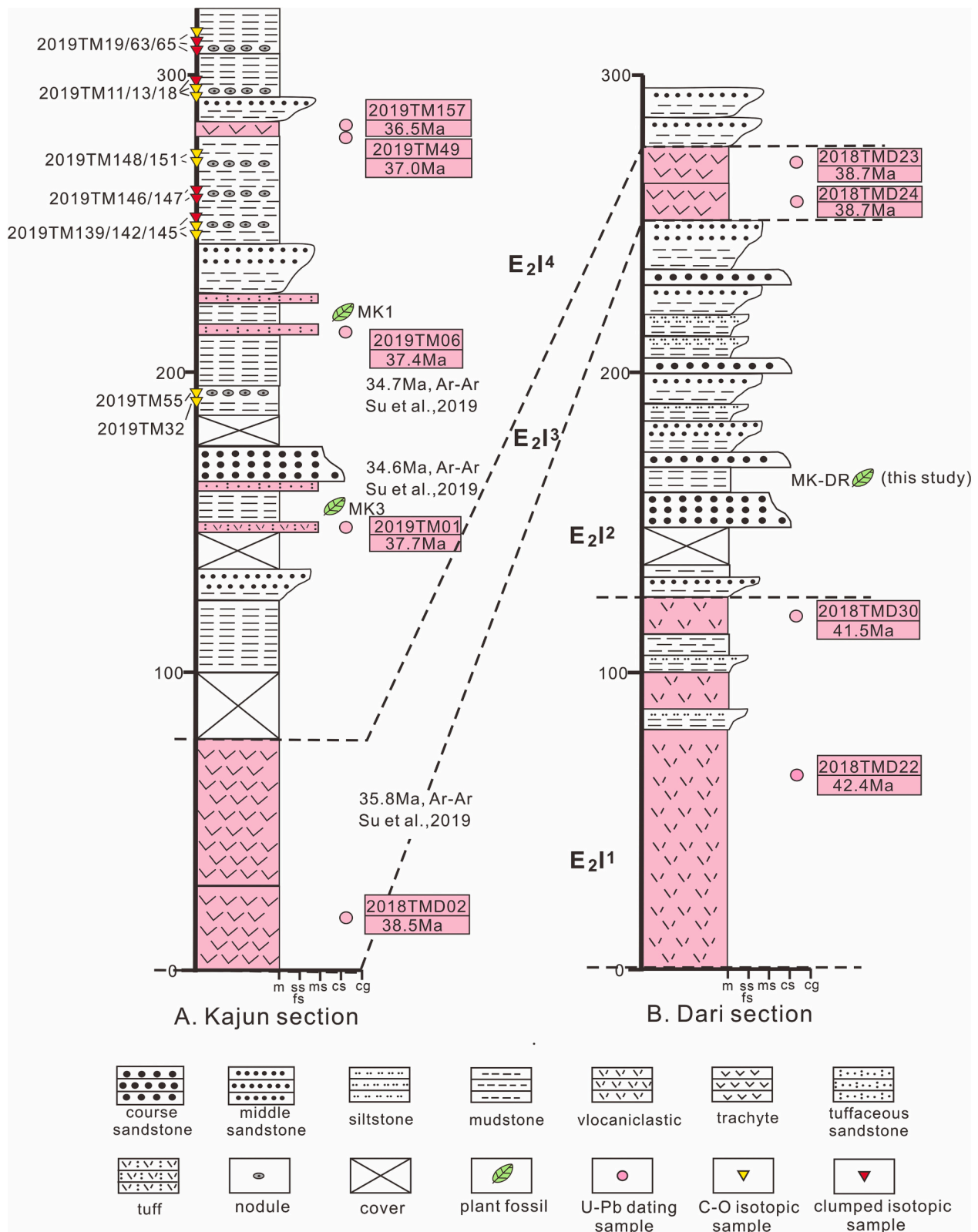
Fig. 3. Measured Kajun and Dari sections in the Markam Basin. The Lawu Fm. is divided into four units with E_2l^1, E_2l^2, E_2l^3 and E_2l^4.

Table S2 and Table S3.

3.3. Nodules sampling and preparation

Fifteen layers of nodules were collected from E_2l^4 in the Kajun section. The samples were picked >40 cm from the exposed paleo-surface to avoid the effects of atmospheric precipitation (Quade et al., 2013). After removing adhering sediment, all the samples for isotopic analysis were selected by eroding a fresh surface that lacked penetrating calcite veins as viewed through a stereomicroscope. Sample powders

were obtained from these fresh surfaces using a low speed microdrill under the stereomicroscope. The selected samples were made into thin sections for mineral analysis and petrographic assessment. X-ray diffraction (XRD) analysis was performed at the Beijing Qingchen Huanyu Petroleum Geological Technology facility to characterize carbonate composition. Petrographic analysis was conducted using scanning electron microscopy (SEM) with energy-dispersive X-ray (EDX) spectroscopy at the Key Laboratory of Orogenic Belts and Crustal Evolution, School of Earth and Space Sciences, Peking University.

3.4. Carbonate stable isotope analysis

Carbon and oxygen isotope analyses were conducted using a Finnigan MAT 253 Isotope Ration Mass Spectrometer with a GasBench II at the Laboratory for Stable Isotope Geochemistry, Institute of Geology and Geophysics, Chinese Academy of Sciences (IGGCAS). Samples were reacted at 72 °C with orthophosphoric acid (specific gravity = 1.85 g/cm^3) in the GasBench II under a helium gas flush. The generated CO_2 was then transferred into a MAT 253. Repeated analysis of the Pee Dee Belemnite (PDB) carbonate standard showed that the laboratory precision for C and O was <0.2‰. The isotope results were reported using standard delta (δ) notation with respect to PDB and expressed as $\delta^{18}O_c$ and $\delta^{13}C_c$ in per mil (‰). All data are available as Table S4.

3.5. Clumped isotope analysis

Clumped isotope (Δ_{47}) analyses were conducted at TPESER. The extraction and purification of CO_2 was performed on a customized vacuum line following the method described in Guo et al. (2019b), Xiong et al. (2022) and Wang et al. (2023). Each 6–8 mg carbonate sample was first reacted with ~1 ml anhydrous phosphoric acid at 90 °C for 15 min to extract CO_2. The produced CO_2 was cleaned through three liquid nitrogen (LN$_2$) traps (−196 °C) and one PoraPak Q trap held at −15 °C to remove moisture and organic contamination.

Purified CO_2 samples were analyzed on a MAT 253 Plus IRMS for Δ_{47} configured to measure m/z 44–49 CO_2, with an additional collector at m/z 47.5 configured to correct the pressure baseline drift in sensitive collectors (m/z 47, 48 and 49). The raw Δ_{47} values were standardized to the Absolute Reference Frame using the heated (1000 °C) gas and equilibrated (25 °C) gas data (Dennis et al., 2011). The offset from acid digestion was corrected through a standard sample transfer function (STF, Chang et al., 2020). The raw data processing steps were finished
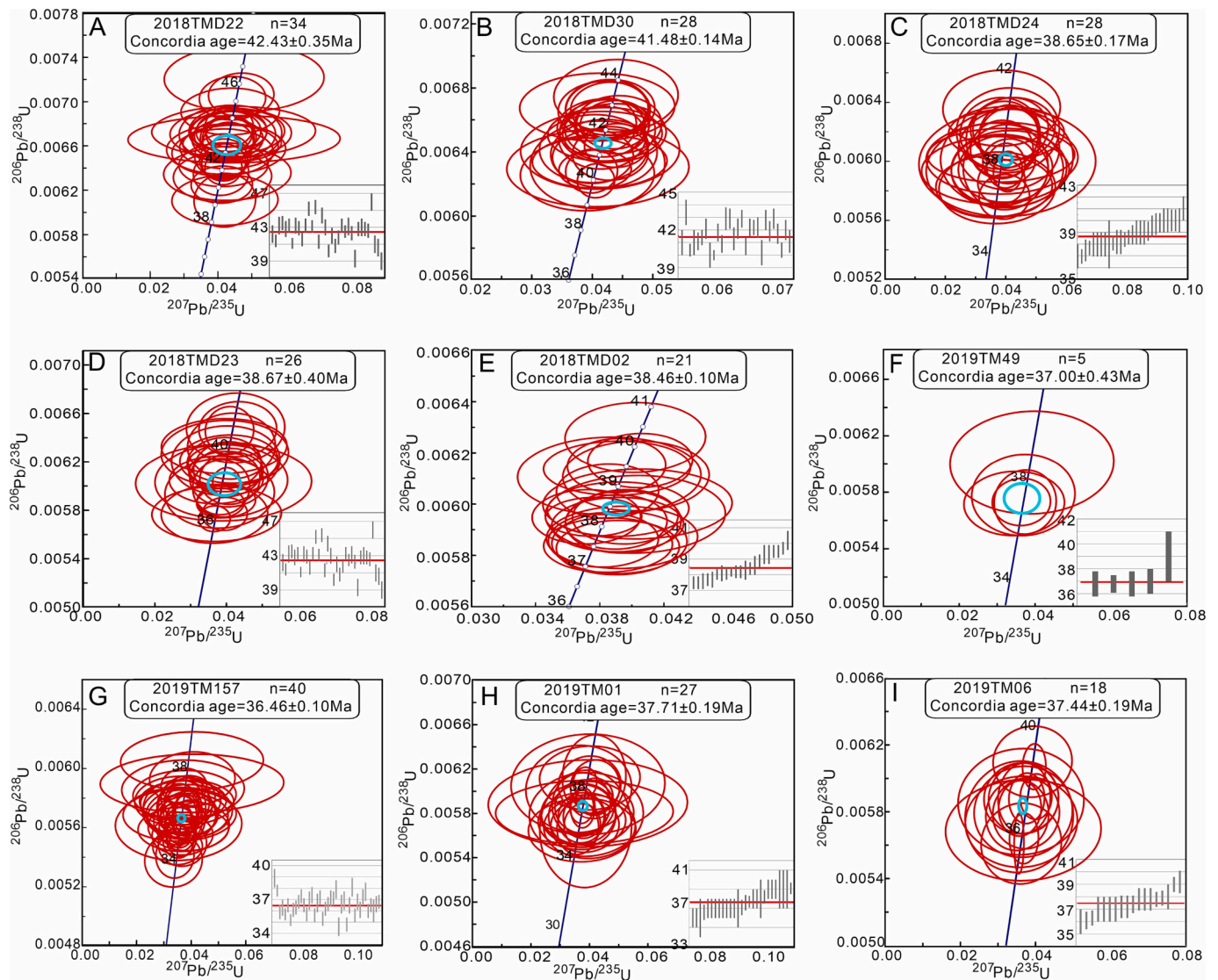

Fig. 4. U − Pb dating results for the Markam Basin. The error bars and ellipses represent 1σ error. A − B. Volcaniclastic samples (2018TMD22, 2018TMD30) in E$_2$l^1; C − E. Trachyte samples (2018TMD24, 2018TMD23, 2018TMD02) in E$_2$l^3; F − G. Trachyte samples (2019TM49, 2019TM157) in the upper part of E$_2$l^4; H. Tuff sample near the MK3 flora (2019TM01); I. Tuffaceous sandstone sample near the MK1 flora (2019TM06).

on "Easotope" software (John and Bowen, 2016). All data are provided in Tables S5 and S6.

4. Results

4.1. Age constraints

Two volcaniclastic samples (2018TMD22, 2018TMD30) collected from E_2l^1 in the Dari Section yield Concordia ages of 42.4 ± 0.4 Ma (1σ, $n = 34$, Fig. 4A) and 41.5 ± 0.1 Ma (1σ, $n = 28$, Fig. 4B), respectively. The dates from the lower volcanic samples constrain the lower age limit of the Lawu Fm. to 42 Ma. Three trachyte samples were collected from E_2l^3 in the Dari and Kajun sections. In the upper part of the Dari section, trachyte samples (2018TMD24, 2018TMD23) yield Concordia ages of 38.7 ± 0.2 Ma (1σ, $n = 28$, Fig. 4C) and 38.7 ± 0.4 Ma (1σ, $n = 26$,

Fig. 4D), respectively. Therefore, the age of MK-DR flora sandwiched between two sets of volcanic rocks at the Dari section is constrained to be 42–39 Ma. The trachyte sample (2018TMD02) from the Kajun section has a Concordia age of 38.5 ± 0.1 Ma (1σ, $n = 21$, Fig. 4E), which is comparable with trachyte ages at the Dari section. Two trachyte samples (2019TM49, 2019TM157) from E_2l^4 near the top of the Kajun section yield Concordia ages of 37.0 ± 0.4 Ma (1σ, $n = 5$, Fig. 4F) and 36.5 ± 0.1 Ma (1σ, $n = 40$, Fig. 4G), and constrain the ages of the nodules within the Kajun section to be 37–36 Ma. In addition, one layer of tuff and one layer of tuffaceous sandstone were collected from the Kajun section, the tuff sample from immediately below MK3 (2019TM01) has a Concordia age of 37.7 ± 0.2 Ma (1σ, $n = 27$, Fig. 4H). The tuffaceous sandstone sample from immediately below MK1 (2019TM06) has a Concordia age of 37.4 ± 0.2 Ma (1σ, $n = 18$, Fig. 4I).
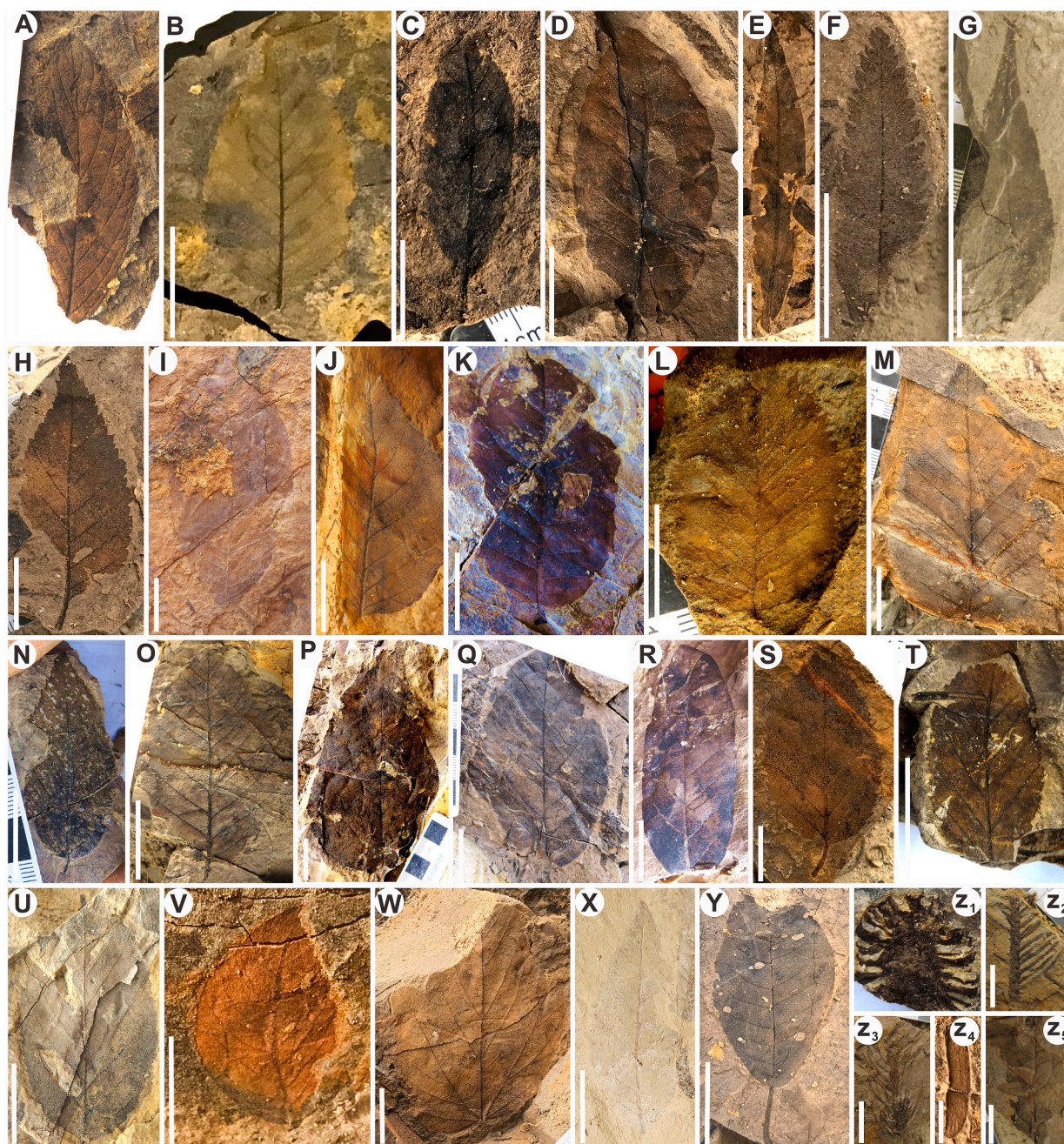

Fig. 5. Representative middle Eocene plant taxa from the Dari section (MK-DR flora). All scale bars are 1 cm in length. E. *Salix*; V. *Populus*; Y. *Quercus*; Z_1. fruit of *Alnus*; Z_2-Z_3. *Pinus*; Z_4. fruit of unknown species; Z_5. Compound leaves.
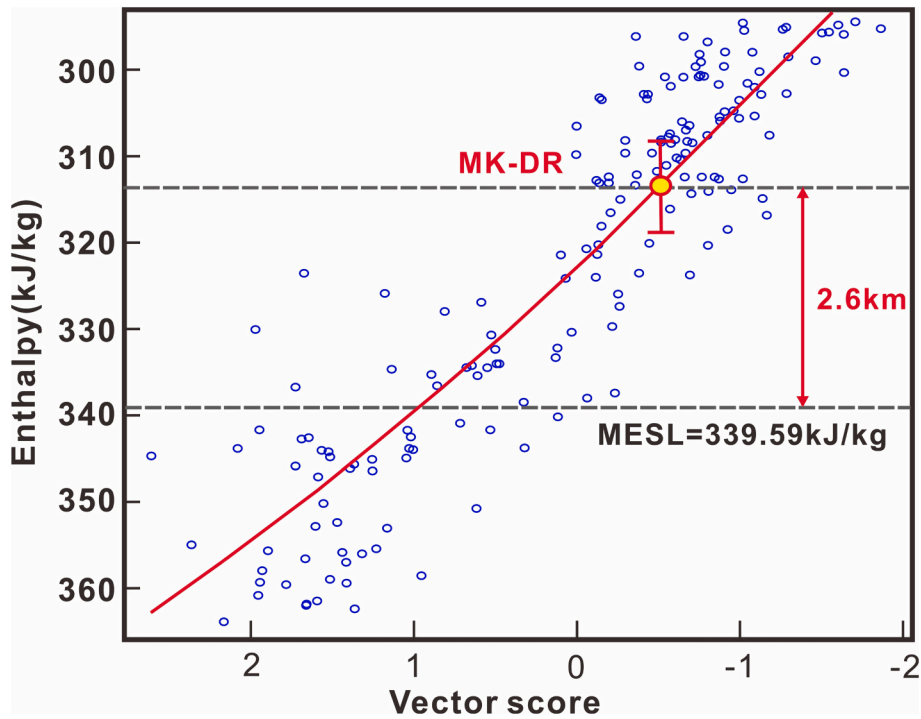
Fig. 6. CLAMP regression plots showing the relationship between moist enthalpy and paleoelevation. The calculation is based on the PhysgAsia2 physiognomic file coupled with the 1-km² resolution gridded climate dataset–WorldClim2 (Fick and Hijmans, 2017). MESL is the moist enthalpy value at sea level. Error bar represents 1σ.
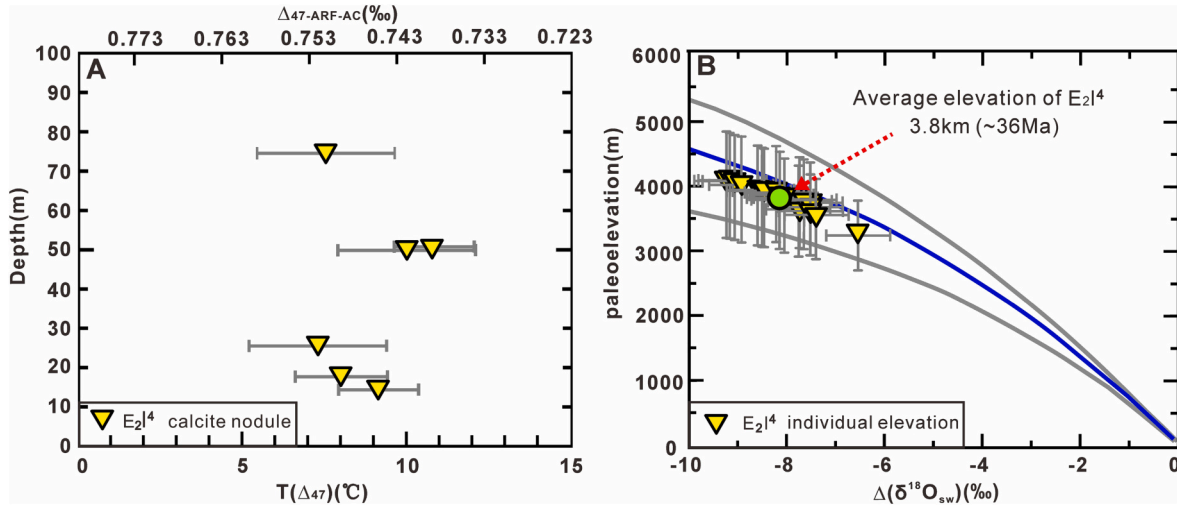

Fig. 7. Clumped isotope results and reconstructed paleoelevation of the Markam Basin. A. Sampling depth of six calcite nodules from E_2l^4 and corresponding $T(\Delta_{47})$ values. B. Paleoelevation reconstructions based on stable and clumped isotope. The green circle represents the average elevation of ~3.8 km. Error bars are 1σ. (For interpretation of the references to colour in this figure legend, the reader is referred to the web version of this article.)

4.2. CLAMP paleoelevation

The physical theory underpinning paleoelevation estimations using CLAMP is based on the observation that moist static energy (*h*) in an air parcel remains conserved as it traverses a mountainous region (Forest et al., 1995). As *h* is mainly the combination of moist enthalpy (*H*) and potential energy (*gZ*, where *g* is gravitational acceleration with a value of 9.81 cm/s², and *Z* is altitude), the elevation of an unknown location can be calculated if we know the difference between *H* at an elevation and that at a contemporaneous sea level site at a similar latitude:

$$Z = \left(H_{\text{sea level}} - H_{\text{fossil site}}\right)/g \tag{1}$$

Analysis of the MK-DR assemblages using the PhysgAsia2 physiognomic data set yield a moist enthalpy value of 314.4 ± 8.4 kJ/kg. To determine the absolute elevation of the MK-DR assemblages, the coeval enthalpy at a known elevation is required. This approach inherently avoids any complications in the elevation calculation due to secular climate change. Paleomagnetism studies of the nearby Gonjo and Nangqian basins have indicated that the eastern Qiangtang terrane was 4–5° south than its present location (Tong et al., 2017). The raw sea-level enthalpy value (336.5 kJ/kg at the paleolocation 25°N, 98°E) is derived from Lutetian climate modeling due to lack of coeval low-elevation floral data (He et al., 2022). The enthalpy values from modeling and proxy data inevitably differ because the model is only an
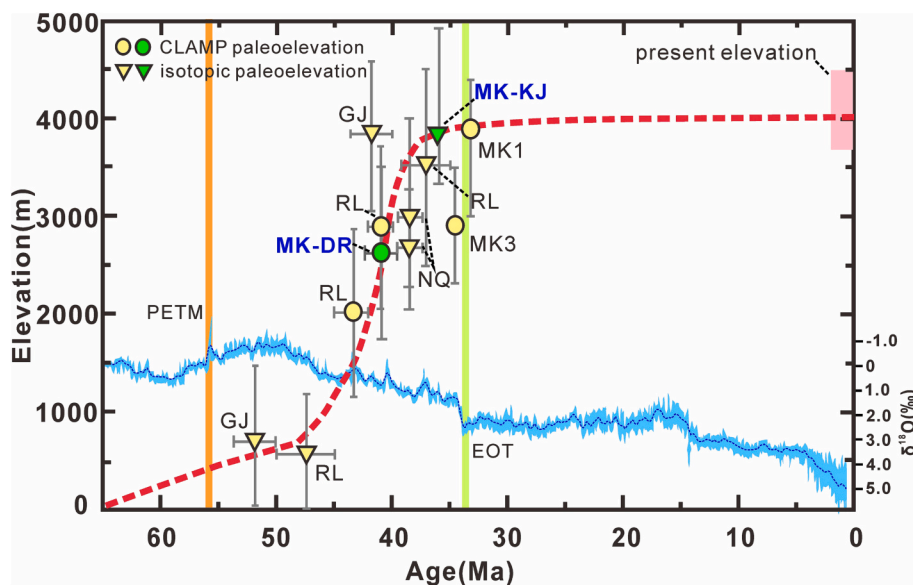
Fig. 8. Reconstructed paleoelevation of the Markam, Gonjo, Relu and Nangqian Basins in the SE Tibet region (He et al., 2022; Li et al., 2018; Su et al., 2019; Xiong et al., 2020). Error bars for individual elevation are 1σ. The circles represent the CLAMP-derived paleoelevation, and the triangles represent oxygen isotope-derived paleoelevation. The green colour represents the Markam Basin, and the yellow colour represents the other adjacent basins. The dashed blue line is the Cenozoic benthic foraminifer oxygen isotope dataset from Westerhold et al. (2020). Abbreviations: GJ, Gonjo Basin; RL, Relu Basin; NQ, Nangqian Basin; PETM, Paleocene-Eocene Thermal Maximum; EOT, Eocene–Oligocene Transition; MK3, MK3 flora from Su et al. (2019); MK1, MK1 flora from Su et al. (2019). MK-DR represents the CLAMP paleoelevation of MK-DR flora. MK-KJ represents the isotopic paleoelevation derived from Kajun section. (For interpretation of the references to colour in this figure legend, the reader is referred to the web version of this article.)
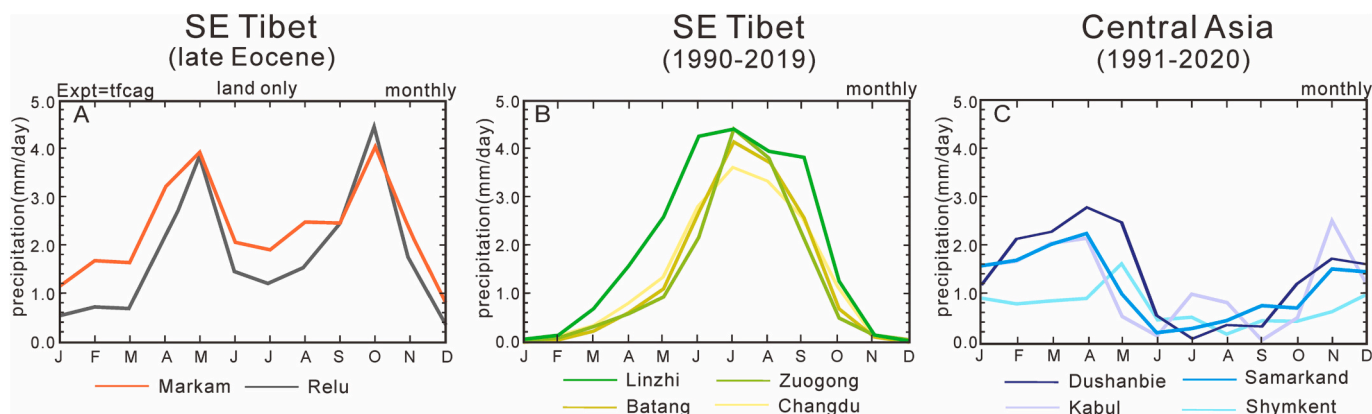

Fig. 9. The seasonal precipitation patterns for the late Eocene SE Tibet, modern SE Tibet and modern Central Asia. A. Modeling results of late Eocene seasonal precipitation (mm/day) across SE Tibet. The orange line represents the Markam Basin, and the gray line represents the Relu Basin. B. Seasonal precipitation (mm/day) of modern SE Tibet (Linzhi, Zuogong, Batang, Changdu), from 1990 to 2019. Data are from China Meteorological Data Service Centre (https://data.cma.cn/). C. Seasonal precipitation (mm/day) of the Mediterranean climate in the modern Central Asia (Dushanbie, Samarkand, Kabul, Shymkent), from 1991 to 2020. Data are from National Oceanic and Atmospheric Administration (http://www.noaa.gov/web.html). Abbreviations: J, January; F, February; M, March; A, April; M: May; J: June; J: July; A: August; S: September; O: October; N: November; D: December. (For interpretation of the references to colour in this figure legend, the reader is referred to the web version of this article.)

approximation to reality, and there are statistical uncertainties inherent in the CLAMP methodology, a latitude-dependent difference regression is used to make model and proxy values compatible (Su et al., 2020). Referring to the empirical calibration line used by Su et al. (2020), sea level moist enthalpy (MESL) from modeling is underestimated by 3.09 kJ/kg. The adjusted enthalpy is 339.59 kJ/kg making the estimated elevation of 2.6 ± 0.9 km for the MK-DR flora (Fig. 6). The uncertainty is a combination of that inherent in CLAMP and model/proxy adjustment.

4.3. Stable isotope paleoelevation

4.3.1. Sample identification

Based on petrographic study and XRD analysis, we divide the samples for paleoelevation determination into siderite-bearing nodules and calcite nodules. Siderite-bearing nodules are yellow or yellowish-brown and 3–10 cm in diameter. XRD and EDX analyses suggest that the main carbonate minerals are calcite, quartz and siderite. Calcite accounts for ~36%–59% and siderite accounts for ~7% of the total composition (see Fig. S3 for 2019TM151, Fig. S4c for 2019TM32). Calcite nodules are slightly smaller with a diameter of 3–5 cm and are yellow in colour (enlarged image Fig. 2E). The petrographic identification reveals a homogeneous character with micrite as the main component, associated with small amount of siliciclastic sediments (Fig. S2). XRD analysis further shows that calcite is the main (at least 70%) carbonate mineral (see Fig. S4a for 2019TM18, Fig. S4b 2019TM19).

4.3.2. Stable and clumped isotope results

Fractionation factors of calcite and siderite are different and cannot be differentiated in bulk stable and clumped isotope analyses (Fernandez et al., 2014; Kelson et al., 2020; Rosenbaum and Sheppard, 1986). Although XRD shows the percentage of siderite mineral in the siderite-bearing nodules is less than ~10%, this is sufficient to cause an apparent temperature change in $T(\Delta_{47})$. Thus, while all the nodules were used for stable isotope analysis, only calcite nodules were selected for clumped isotope analysis. The oxygen isotope values ($\delta^{18}O_c$) of nine siderite-bearing nodules range from −15.3‰ to −13.9‰ with an average value of −14.7 ± 0.5‰ (1σ, $n = 9$, Table S4). The carbon isotope values range from −4.5‰ to 2.8‰ with an average value of −2.0 ± 2.6‰ (1σ, $n = 9$, Table S4). Six calcite nodules yield oxygen isotopic values ($\delta^{18}O_c$) ranging from −14.33‰ to −13.46‰, with an average value of −13.9 ± 0.3‰ (1σ, $n = 6$, Table S4). The carbon isotope values range from −6.2‰ to −3.6‰, with an average value of −5.1 ± 0.9‰ (1σ, $n = 6$, Table S4).

Six calcite nodules yield Δ_{47} values ranging from 0.740‰ to 0.756‰, with an average value of 0.747 ± 0.004‰ (1σ, $n = 6$, Table S5). Based on similar sample types and large temperature coverage, the calibration equation of Kelson et al. (2017) is used to deduce the carbonate formation temperature. The calculated temperatures range from 7.3 ± 2.7 °C to 10.8 ± 1.2 °C with an average value of 8.6 ± 1.2 °C (1σ, $n = 6$, Fig. 7A). For comparison, several recent calibrations (Anderson et al., 2021; Meinicke et al., 2021; Petersen et al., 2019) are used to calculate the temperature and the detailed results are listed in Table S5. This shows the temperature difference between different calibrations is <3 °C, and within the range of measurement uncertainty.

4.3.3. Diagenesis assessment

The primary $\delta^{18}O$ value of authigenic carbonate minerals is highly susceptible to post-depositional alteration via mineral dissolution-reprecipitation or diffusional mass exchange with pore water or other phases (Huntington and Lechler, 2015). The overprinted values will lead to erroneous paleoelevation estimates. Here, we use petrographic analysis, XRD analysis, SEM with EDX tests, coupled with clumped isotope thermometry, to evaluate potential diagenetic effects.

Petrographic study suggests that the calcite nodules are dominated by micrite, associated with minor siliciclastic sediments. SEM with EDX investigations show a low content of crystallographic siderite. Diagenetic fabrics of sparry or filled vein calcite are rare (Fig. S2). XRD analysis also suggests the dolomite content is <3%, indicating that samples have not undergone obvious recrystallization or late dolomitization.

$T(\Delta_{47})$ of the six calcite nodules from the Lawu Fm. of the Markam Basin range from 7.3 °C to 10.8 °C, which is below the upper limit of surface carbonate formation temperature (40 °C) in mid-latitude areas (Quade et al., 2013). This low temperature is also below the lower temperature limit (100 °C) for solid-state reordering on a 1–100 Ma timescale and so preserves the original formation temperature (Henkes et al., 2014). Coupled with petrographic analysis, XRD analysis, SEM with EDX tests, we conclude that the nodules in the Markam Basin preserve original temperature and oxygen isotope information for paleoelevation determination.

4.3.4. Stable isotope paleoelevation calculation

In simple systems featuring air rising against a single mountain barrier, stable isotopes in ascending air parcels are depleted systematically with increasing altitude. The topographic barrier causes water vapor to condense following a process of Rayleigh distillation (Rowley, 2007). In the SE Tibet area, the distinctive monsoon-dominated climate of today reflects the interaction of both the South Asian Monsoon (SAM) and East Asian Monsoon (EAM), and published $\delta^{18}O_{SW}$ data from IAEA-GNIP station, stream, lake and spring waters have demonstrated the application of stable isotope paleoaltimetry even in the complex environment of SE Tibet (Hoke et al., 2014; Hoke, 2018; Li et al., 2018).

Proxy-derived and paleoclimate modeling results from the nearby Gonjo and Relu basins showed that in the late Eocene the main moisture source was the ocean south of Asia (He et al., 2022; Xiong et al., 2020). The average $\delta^{18}O$ value of GNIP station (New Delhi) is −5.9 ± 1‰. Because of global cooling since the Eocene and the formation of continental ice sheets, there is an enrichment of $\delta^{18}O$ values of at least +1.2‰ over those of the Eocene (Meckler et al., 2022; Westerhold et al., 2020). As a result, the adjusted $\delta^{18}O_{SW}$ value at low elevation is −7.1‰. This is comparable with the mean $\delta^{18}O$ value of surface water derived from late Eocene gastropod shells from the low elevation Myanmar Basin, which is −7.2 ± 1‰ (Licht et al., 2014).

Combining the $T(\Delta_{47})$ and the fractionation equation from Kim and O'Neil (1997), the calculated oxygen isotope values ($\delta^{18}O_{SW}$) within calcite nodules are in the range of −15.3‰ to −14.1‰. For comparison, the $\delta^{18}O_{SW}$ values of nine siderite nodules, using the average $T(\Delta_{47})$ from calcite nodules, vary from −16.7‰ to −15.2‰.

The paleolatitude effects need to be corrected for in any application of oxygen isotope paleoaltimetry. As mentioned previously, paleomagnetic work in the nearby Nangqian Basin indicated a 4–5° northward movement of the eastern Qiangtang terrane since the middle Eocene (Tong et al., 2017), so we apply a 4° southward latitudinal shift to the Markam Basin that yields an enrichment value of +0.5‰ (Bowen and Wilkinson, 2002). After considering this palaeolatitudinal difference, the calculated values of $\delta^{18}O_{sw}$ range from −16.2‰ to −13.6‰. Subtracted from the low elevation reference $\delta^{18}O_{SW}$, the values of $\Delta^{18}O_{mw}$ range from −9.1‰ to −6.5‰ with an average value of −8.0‰. When we employ the fractionation model of Rowley (2007), and considering the modeling uncertainties and propagated uncertainties (the low elevation moisture source, $\delta^{18}O_c$, $T(\Delta_{47})$), the latest Eocene paleoelevation of Markam Basin is within the range of 3315 (+514/−667) m to 4095 (+723/−895) m and the average value is 3801 (+649/−815) m (Fig. 7B, Table S7).

4.4. Proxy-derived paleoclimate

The CLAMP derived paleoclimate estimates for the middle Eocene (ca. 42–39 Ma) MK-DR yield a MAAT of 13.16 ± 2.36 °C, with a warm month mean temperature (WMMT) of 24.45 ± 2.91 °C and a cold-month mean temperature (CMMT) of 2.44 ± 3.54 °C. The length of growing seasons (LGS) is estimated to have been 8.26 ± 1.09 months. The growing season precipitation (GSP) was 1762.9 ± 643.2 mm, while precipitation during the three consecutive wettest months (3WET) was 871.7 ± 400.4 mm and the dry season (3DRY) estimate is 272.6 ± 98.2 mm, making the ratio between the wet and dry season precipitation of 3:1. The relative humidity (RH) is estimated to have been 66.21 ± 10.14% and the specific humidity (SH) was 7.19 ± 1.77 g/kg. The vapor pressure deficit (VPD) was highest (driest) in summer at 8.05 ± 3.47 hPa, while it was lowest (wettest) in winter at 2.40 ± 1.52 hPa.

5. Discussion

5.1. Revised age of the Markam Basin

A precise chronostratigraphic framework is the basis for any discussion of surface uplift and linking of climatic events. Nine newly obtained dates for volcanic rocks occurring within the Markam Basin are used to construct the dating framework of the Lawu Fm.. Two volcaniclastic samples from the lower part of the succession at the Dari section constrain the maximum depositional age of E_2l^1 to 42.4 Ma. The Concordia ages of three trachyte samples constrain the overlying E_2l^3 to 38.7–38.5 Ma. Thus, the E_2l^2 and MK-DR flora between E_2l^1 and E_2l^3 are constrained to 42.4–38.5 Ma. Two trachyte samples from the uppermost Kajun section have Concordia ages of 37.0 Ma and 36.5 Ma respectively, which implies the age of E_2l^4 was not younger than 36.5 Ma. The tuff sample (2019TM01) and the layer of tuffaceous sandstone (2019TM06) yield ages of 37.7 Ma and 37.4 Ma and constrain the age of E_2l^4 to

between 38.5 Ma and 36.5 Ma.

Originally the plant assemblages from the Lawu Fm. were assumed to be Late Miocene based on floral similarity to those of the Gazhacun Fm. in the Namling Basin (Guo et al., 2019a; Tao and Du, 1987). However, radiometric dating refined the age of the Lawu Fm. flora to late Eocene−early Oligocene. Zhang et al. (2005) reported that the $^{40}Ar - ^{39}Ar$ ages of high-K volcanic rocks in Kajun village formed at 33.5 ± 0.2 Ma. Su et al. (2019) also constrained the MK3 and MK1 leaf floras of Lawu Fm. to be 35.5 ± 0.3 to 33.4 ± 0.5 Ma using the $^{40}Ar - ^{39}Ar$ approach. However, $U - Pb$ ages of zircon constrain the age of E_2l^4 to be in the range of 38.5–36.5 Ma which is 2–3 Ma older than those from $^{40}Ar - ^{39}Ar$ dating (Su et al., 2019; Zhang et al., 2005). The discrepancy is within the measurement uncertainty of $U - Pb$ and $^{40}Ar - ^{39}Ar$ dating, which could represent the differences inherent in the dating methods themselves, or sample heterogeneity, or reflect the different closure temperatures of the minerals used for the different analyses. The detailed methodology comparison is out of the scope of this study and in order to keep data consistency, we discuss the elevation history within the dating framework constructed by our $U - Pb$ results.

5.2. The late Eocene rise of SE Tibet and Paleogene topography of THH highlands

The MK-DR flora, integrated with stable isotope analysis, depicts the uplift history of the Markam Basin. Our work shows that the Markam Basin remained at a moderate elevation (2.6 ± 0.9 km) at ca. 42–39 Ma. The basin then rose rapidly to 3.8 (+0.6/−0.8) km by 36 Ma as indicated by oxygen isotope paleoaltimetry, which is identical with the 3.9 ± 0.9 km of leaf physiognomy (MK1) result within uncertainty (Su et al., 2019). The uplift rate was around 0.17 mm/yr at 42–36 Ma. Thermochronological data obtained in the Markam Basin showed a cooling episode at ca. 40–35 Ma, which coincides with the time of surface elevation rise (Cao et al., 2022).

Stable isotope paleoaltimetry for the Gonjo Basin indicated uplift from 0.7 km to 3.8 km during the middle Eocene (Xiong et al., 2020). Combined CLAMP and clumped isotope results for the Relu Basin in the Yidun Arc indicate a rise in elevation from 0.6 km to 3.7 km between 45 Ma and 34 Ma (He et al., 2022). The uplift rate was 0.5 mm/yr for the Gonjo Basin and 0.28 mm/yr for the Relu Basin, and so faster than that of the Markam Basin. All these paleoelevation results plus others, such as the Jianchuan Basin (Wu et al., 2018), indicate a high SE Tibetan margin (~3.0 km) formed during the late Eocene (Fig. 8). Tao et al. (2022) reviewed the thermochronological evidence from SE Tibet and found that Eocene to early Oligocene cooling episode is pervasive across the region. Contemporaneous thrusting and adakite magmatism in SE Tibet suggested that crustal shortening and upwelling of metasomatized mantle magma are possible dynamic drivers for such a surface rise (Horton et al., 2002; Spurlin et al., 2005; Wang et al., 2022).

Incorporated with the elevation history of SE Tibet, a clear Paleogene elevation history of THH emerges. The Gangdese and Watershed Mountains were elevated to an altitude of 4.5 km at ca. 60–50 Ma (Ding et al., 2014; Ibarra et al., 2023; Xu et al., 2013, 2022), whereas the zone between them remained at low elevation, forming a wide Central Tibetan Valley (Ding et al., 2014, 2022; Su et al., 2020; Xiong et al., 2022). During 40–30 Ma, the demise of the Central Tibetan Valley marked the formation of a latest Paleogene plateau-like topography (Xiong et al., 2022), albeit still with a central lake-filled depression, and uplift continued into the Miocene (Li et al., 2022). SE Tibet also gained substantial elevation just prior to the demise of the Central Tibet Valley in middle to late Eocene time to became the high late Paleogene to earliest Neogene near-modern plateau (He et al., 2022; Hoke, 2018; Li et al., 2018; Xiong et al., 2020; this study).

5.3. The development of a late Eocene Mediterranean-like climate in SE Tibet

During the late Eocene, increasing evidence suggests that a primitive climate system, but distinct from the present, began to dominate SE Tibet and adjacent areas (He et al., 2022). In the Markam Basin, the MK-DR, MK3 and MK1 floras represent subtropical vegetation becoming deciduous-broadleaved and more coniferous over time (Su et al., 2019; this study). The precipitation signal of the MK-DR flora shows rainfall to have been in excess of 1700 mm during an 8-month growing period, similar with that at ~37.7 Ma when the MK3 flora shows it to have been in excess of 2000 mm, but over a longer 10 months growing season. Moderate drying had apparently occurred by ~37.4 Ma as MK1 shows 1704 mm for a 9.7-month growing season. The CLAMP-derived ratio between the three wettest months and the three driest months was 3.1:1 for MK-DR, indicating moderate seasonal variability. The representative TR1 and TR3 floras in the Relu Basin revealed a biodiverse subtropical evergreen broad-leaved forest with a high precipitation ratio between the three wettest months and the three driest months (7:1, 6:1). In addition, stable isotope analysis of fossil mammal teeth in the Relu Basin and gastropod growth lines in the Jianchuan Basin suggest seasonal variations (Fang et al., 2021; He et al., 2022), but this does not define when in the year the wet season occurred, and in the absence of other information it has been assumed that the climate was summer-wet as it is today. Previous numerical climate modeling shows the Eocene climate system in SE Tibet was quite different to that seen as present (Fang et al., 2021; He et al., 2022). Specifically, He et al. (2022) demonstrated that the rise of eastern Tibet had little effect on summer month precipitation, but led to enhanced humidity during the winter when most moisture was available to plants.

In our study, the rise of SE Tibet produces a unique Mediterranean-like climate, in that a bi-modal precipitation system developed with two peaks, one during the spring (MAM) and one during the autumn (SON) (> 4–5 mm/day, Fig. 9A), with lower precipitation in the winter (DJF) and summer (JJA) seasons (< 2 mm/day, Fig. 9A). This is like the modern Mediterranean climate, which is characterized by warm and dry summers (JJA), while the cool rainy season lasts from late autumn to spring (Huang et al., 2013; Fig. 9C). Another line of evidence that supports the Mediterranean-like climate comes from the plant fossils, in that a typical semi-arid or arid flora that includes palm leaves, 'Eucalyptus', *Palibinia, Quercus* sp. and *Hippophae* sp. shows some similarity to Mediterranean vegetation. The paleo-flora co-evolved with the rise of SE Tibet, and even dispersed to the southern China (Guo, 1978; He et al., 2022; Sun and Li, 2003; Zhou et al., 2023). This special Mediterranean climate is at odds with the larger-scale monsoon system over East Asia today that exhibits a summer-dominated uni-modal precipitation pattern (Fig. 9B), but is consistent with available local CLAMP-based proxy evidence from leaf mega-fossils from the late Eocene Relu and Markam basins.

Seasonal wind patterns at 850 hPa also show clear differences with those of the present. During the late Eocene, once SE Tibet has risen to its current elevation, there is no seasonal wind reversal as seen today (Fig. S5). We take from this that climate dynamics are strongly related to topographic evolution and change through time, meaning there is no time in the past when the modern monsoon system suddenly 'switched on'. Rather, monsoon evolution was gradual and it is misleading to refer the Asian Monsoon this far back in time, because to do so implies that the modern circulatory and rainfall pattern existed as early as the Eocene when regional orography was very different and highly dynamic. There are many important geological and climatic events that have profoundly affected the Asian climate framework since the Eocene, like the rise of the Himalaya Mountains, the existence of a Central Tibetan Valley, the growth of northern Tibet, the retreat of Paratethys and global cooling (Ding et al., 2017; Li and Garzione, 2023; Sun et al., 2020; Westerhold et al., 2020; Xiong et al., 2022). As a result, the timing and mechanics underpinning the establishment of the modern Asian

monsoon system are still an open question. What we have shown here is that during the orographic development of the THH, the Asian monsoon system exhibited a range of characteristics that were different to those of the present and that it evolved in a complex way, with profound implications for further development of paleoaltimetric tools and our understanding of the history of biodiversity in Asia.

A Mediterranean-like climate, which is spring-autumn-wet, developed in parts of southern Asian during the late Eocene. This climate dominated SE Tibet and surrounding regions. During the late Eocene, the Paratethys was located at a latitude of 25–40°N and longitude of 40–80°E (Bougeois et al., 2018; Licht et al., 2014; Sun et al., 2020). The bi-model precipitation peaks in SE Tibet seems to have been influenced by the moisture from the west sourced from the Paratethys, flowed around the Gangdese and Qiangtang highland (Ding et al., 2014; Ibarra et al., 2023; Xu et al., 2013, 2022). It has also been demonstrated that elevated topography generates more water-rich ascent from low elevations (Kirshbaum and Grant, 2012). In this case, the low elevation area was the south of eastern Tibet (He et al., 2022). The ascent of a moist air parcel forces condensation and subsequent precipitation due to localized disturbance and blocking effects of mountains (Barros and Lettenmaier, 1994). As a result, the surface rise of SE Tibet caused an intensification of seasonal rainfall, which in turn amplified seasonal changes in temperature, enhancing weathering and contributing to extensive river incision across SE Tibet to form the high relief, high biodiversity province of the modern Hengduan Mountains. These topographic scenarios highlight the importance of having realistic topographic configurations in climate models mediated by proxy evidence. Atmospheric circulation and precipitation patterns in the Tibetan region are primarily driven by complex regional topographic development and not the rise of Tibet as one monolithic block, as has often been modelled. Moreover, the tectonic model in which a proto-Tibetan Plateau has existed since at least the middle Eocene (Botsyun et al., 2019; Li et al., 2019; Mulch and Chamberlain, 2006; Wang et al., 2014; Wei et al., 2022; Zhu et al., 2019) is incompatible with the recent observations in central Tibet (Su et al., 2020; Xiong et al., 2022). The Paleogene proto-Tibetan Plateau theory is mainly a result of stable isotope paleoaltimetry that has been used extensively for decades, but which cannot resolve inter-montane lowlands (Farnsworth et al., 2023; Spicer et al., 2021). While stable isotope paleoaltimetry works well in the case of the initial ascent of an air parcel over a mountain, the depleted signal is preserved in the air parcel on the lee-side of a mountain (Deng and Jia, 2018) and so yields a 'phantom plateau' signal in an inter-montane basin (Spicer et al., 2021). More data at basinal scale is required to better constrain and understand the uplift history of the THH highlands to reduce uncertainty in elevation histories. This will aid the formulation of more robust paleogeographic reconstructions for use in paleoclimate models, allowing more legitimate testing against geologic proxies and in turn improving those proxies.

6. Conclusions

A knowledge of the topographic growth of SE Tibet is crucial for understanding fully the differential uplift history of the whole THH highlands, links between climate development and biodiversity evolution not just in Asia, but globally. Sedimentary analysis and U − Pb ages of volcaniclastic rocks establish a chronostratigraphic framework for the Lawu Fm. in the Markam Basin across an age range from 42 Ma to 36 Ma. A combination of paleoelevation proxies based on the newly-discovered MK-DR leaf fossil assemblage and stable isotope measurements show that the paleoelevation of the Markam Basin floor was at 2.6 km at ca. 42–39 Ma, then rose to its present elevation (3.8 km) at ~36 Ma. Integrated with previous paleoaltimetry research, we conclude that SE Tibet, as a whole, underwent a rapid growth during the Paleogene to form the current high-elevation topography. This initially near-planar surface was subsequently heavily dissected through drainage development and weathering under a 'Mediterranean' climate that the rise of SE

Tibet itself created. River incision generated high topographic relief which in turn enhanced speciation and biodiversity.

Declaration of Competing Interest

The authors declare that they have no conflict of interests.

Data availability

All data were available in Appendix A Supplementary data.

Appendix A. Supplementary data

Supplementary data to this article can be found online at https://doi.org/10.1016/j.gloplacha.2023.104313.

References

Andersen, T., 2002. Correction of common lead in U−Pb analyses that do not report 204Pb. Chem. Geol. 192, 59–79. https://doi.org/10.1016/S0009-2541(02)00195-X.

Anderson, N.T., Kelson, J.R., Kele, S., Daëron, M., Bonifacie, M., Horita, J., Mackey, T.J., John, C.M., Kluge, T., Petschnig, P., Jost, A.B., Huntington, K.W., Bernasconi, S.M., Bergmann, K.D., 2021. A unified clumped isotope thermometer calibration (0.5-1, 100°C) using carbonate-based standardization. Geophys. Res. Lett. 48 https://doi.org/10.1029/2020GL092069 e2020GL092069.

Antonelli, A., Kissling, W.D., Flantua, S.G., Bermúdez, M.A., Mulch, A., Muellner-Riehl, A.N., Kreft, H., Linder, H.P., Badgley, C., Fjeldså, J., Fritz, S.A., Rahbek, C., Herman, F., Hooghiemstra, H., Hoorn, C., 2018. Geological and climatic influences on mountain biodiversity. Nat. Geosci. 11, 718–725. https://doi.org/10.1038/s41561-018-0236-z.

Barros, A.P., Lettenmaier, D.P., 1994. Dynamic modeling of orographically induced precipitation. Rev. Geophys. 32, 265–284. https://doi.org/10.1029/94RG00625.

Botsyun, S., Sepulchre, P., Donnadieu, Y., Risi, C., Licht, A., Caves Rugenstein, J.K., 2019. Revised paleoaltimetry data show low Tibetan Plateau elevation during the Eocene. Science 363, eaaq1436. https://doi.org/10.1126/science.aaq1436.

Bougeois, L., Dupont-Nivet, G., de Rafélis, M., Tindall, J.C., Proust, J.-N., Reichart, G.-J., de Nooijer, L.J., Guo, Z., Ormukov, C., 2018. Asian monsoons and aridification response to Paleogene Sea retreat and Neogene westerly shielding indicated by seasonality in Paratethys oysters. Earth Planet. Sci. Lett. 485, 99–110. https://doi.org/10.1016/j.epsl.2017.12.036.

Bowen, G.J., Wilkinson, B., 2002. Spatial distribution of δ18O in meteoric precipitation. Geology 30, 315–318. https://doi.org/10.1130/0091-7613(2002)030<0315:SDOOIM>2.0.CO;2.

Burchfiel, B.C., Chen, Z., 2012. Tectonics of the southeastern Tibetan Plateau and its adjacent foreland. Geol. Soc. Am. Bull. U.S.A. 210, 1–164.

Cao, K., Wang, G., Leloup, P.H., Mahéo, G., Xu, Y., van der Beek, P.A., Replumaz, A., Zhang, K., 2019. Oligocene–Early Miocene topographic relief generation of southeastern Tibet triggered by thrusting. Tectonics 38, 374–391. https://doi.org/10.1029/2017TC004832.

Cao, K., Tian, Y., van der Beek, P., Wang, G., Shen, T., Reiners, P., Bernet, M., Husson, L., 2022. Southwestward growth of plateau surfaces in eastern Tibet. Earth Sci. Rev. 232, 104160 https://doi.org/10.1016/j.earscirev.2022.104160.

Chang, B., Defliese, W.F., Li, C., Huang, J., Tripati, A., Algeo, T.J., 2020. Effects of different constants and standards on the reproducibility of carbonate clumped isotope (Δ47) measurements: Insights from a long-term dataset. Rapid Commun. Mass Spectrom. 34, e8678 https://doi.org/10.1002/rcm.8678.

Chen, Y., Wu, B., Xiong, Z., Zan, J., Zhang, B., Zhang, R., Xue, Y., Li, M., Li, B., 2021. Evolution of eastern Tibetan river systems is driven by the indentation of India. Commun. Earth Environ. 2, 256. https://doi.org/10.1038/s43247-021-00330-4.

Clark, M.K., Royden, L.H., 2000. Topographic ooze: building the eastern margin of Tibet by lower crustal flow. Geology 28, 703–706. https://doi.org/10.1130/0091-7613(2000)28<703:Tobtem>2.0.Co;2.

Clark, M.K., Schoenbohm, L.M., Royden, L.H., Whipple, K.X., Burchfiel, B.C., Zhang, X., Tang, W., Wang, E., Chen, L., 2004. Surface uplift, tectonics, and erosion of eastern Tibet from large-scale drainage patterns. Tectonics 23, TC1006. https://doi.org/10.1029/2002tc001402.

Clark, M.K., Bush, J.W.M., Royden, L.H., 2005. Dynamic topography produced by lower crustal flow against rheological strength heterogeneities bordering the Tibetan Plateau. Geophys. J. Int. 162, 575–590. https://doi.org/10.1111/j.1365-246X.2005.02580.x.

Clark, M.K., Royden, L.H., Whipple, K.X., Burchfiel, B.C., Zhang, X., Tang, W., 2006. Use of a regional, relict landscape to measure vertical deformation of the eastern Tibetan Plateau. J. Geophys. Res. Earth Surf. 111, F03002. https://doi.org/10.1029/2005JF000294.

Deng, L., Jia, G., 2018. High-relief topography of the Nima basin in central Tibetan Plateau during the mid-Cenozoic time. Chem. Geol. 493, 199–209. https://doi.org/10.1016/j.chemgeo.2018.05.041.

Dennis, K.J., Affek, H.P., Passey, B.H., Schrag, D.P., Eiler, J.M., 2011. Defining an absolute reference frame for 'clumped' isotope studies of CO_2. Geochim. Cosmochim. Acta 75, 7117–7131. https://doi.org/10.1016/j.gca.2011.09.025.

Ding, L., Xu, Q., Yue, Y., Wang, H., Cai, F., Li, S., 2014. The Andean-type Gangdese Mountains: paleoelevation record from the Paleocene–Eocene Linzhou Basin. Earth Planet. Sci. Lett. 392, 250–264. https://doi.org/10.1016/j.epsl.2014.01.045.

Ding, L., Spicer, R.A., Yang, J., Xu, Q., Cai, F., Li, S., Lai, Q., Wang, H., Spicer, T.E.V., Yue, Y., Shukla, A., Srivastava, G., Khan, M.A., Bera, S., Mehrotra, R., 2017. Quantifying the rise of the Himalaya orogen and implications for the South Asian monsoon. Geology 45, 215–218. https://doi.org/10.1130/g38583.1.

Ding, W.-N., Ree, R.H., Spicer, R.A., Xing, Y.-W., 2020. Ancient orogenic and monsoon-driven assembly of the world's richest temperate alpine flora. Science 369, 578–581. https://doi.org/10.1126/science.abb4484.

Ding, L., Kapp, P., Cai, F., Garzione, C.N., Xiong, Z., Wang, H., Wang, C., 2022. Timing and mechanisms of Tibetan Plateau uplift. Nat. Rev. Earth Environ. 3, 652–667. https://doi.org/10.1038/s43017-022-00318-4.

Fang, X., Dupont-Nivet, G., Wang, C., Song, C., Meng, Q., Zhang, W., Nie, J., Zhang, T., Mao, Z., Chen, Y., 2020. Revised chronology of Central Tibet uplift (Lunpola Basin). Sci. Adv. 6, eaba7298. https://doi.org/10.1126/sciadv.aba7298.

Fang, X., Yan, M., Zhang, W., Nie, J., Han, W., Wu, F., Song, C., Zhang, T., Zan, J., Yang, Y., 2021. Paleogeography control of Indian monsoon intensification and expansion at 41 Ma. Sci. Bull. 66, 2320–2328. https://doi.org/10.1016/j.scib.2021.07.023.

Farnsworth, A., Lunt, D.J., Robinson, S.A., Valdes, P.J., Roberts, W.H.G., Clift, P.D., Markwick, P., Su, T., Wrobel, N., Bragg, F., Kelland, S.-J., Pancost, R.D., 2019. Past East Asian monsoon evolution controlled by paleogeography, not CO_2. Sci. Adv. 5, eaax1697. https://doi.org/10.1126/sciadv.aax1697.

Farnsworth, A., Valdes, P.J., Ding, L., Spicer, R.A., Li, S.H., Su, T., Li, S., Witkowski, C.R., Xiong, Z., 2023. Limits of oxygen isotope palaeoaltimetry in Tibet. Earth Planet. Sci. Lett. 606, 118040 https://doi.org/10.1016/j.epsl.2023.118040.

Fernandez, A., Tang, J., Rosenheim, B.E., 2014. Siderite 'clumped' isotope thermometry: a new paleoclimate proxy for humid continental environments. Geochim. Cosmochim. Acta 126, 411–421. https://doi.org/10.1016/j.gca.2013.11.006.

Fick, S.E., Hijmans, R.J., 2017. WorldClim 2: new 1-km spatial resolution climate surfaces for global land areas. Int. J. Climatol. 37, 4302–4315. https://doi.org/10.1002/joc.5086.

Forest, C.E., Molnar, P., Emanuel, K.A., 1995. Palaeoaltimetry from energy conservation principles. Nature 374, 347–350. https://doi.org/10.1038/374347a0.

Guo, S.X., Spicer, R.A., Widdowson, M., Herman, A.B., Domogatskaya, K.V., 2019a. The composition of the middle Miocene (15 Ma) *Namling paleoflora*, South Central Tibet, in the context of other Tibetan and Himalayan Floras. Rev. Palaeobot. Palynol. 271, 104088 https://doi.org/10.1016/j.revpalbo.2019.06.011.

Guo, S.X., 1978. Pliocene Flores of western Sichuan. Acta Palaeontol. Sin. 3, 343–349 (in Chinese with English abstract).

Guo, Y., Deng, W.F., Wei, G., 2019b. Kinetic effects during the experimental transition of aragonite to calcite in aqueous solution: insights from clumped and oxygen isotope signatures. Geochim. Cosmochim. Acta 248, 210–230. https://doi.org/10.1016/j.gca.2019.01.012.

Guo, Z.T., Sun, B., Zhang, Z.S., Peng, S.Z., Xiao, G.Q., Ge, J.Y., Hao, Q.Z., Qiao, Y.S., Liang, M.Y., Liu, J.F., Yin, Q.Z., Wei, J.J., 2008. A major reorganization of Asian climate by the early Miocene. Clim. Past 4, 153–174. https://doi.org/10.5194/cp-4-153-2008.

He, S., Ding, L., Xiong, Z., Spicer, R.A., Farnsworth, A., Valdes, P.J., Wang, C., Cai, F., Wang, H., Sun, Y., Zeng, D., Xie, J., Yue, Y., Zhao, C., Song, P., Wu, C., 2022. A distinctive Eocene Asian monsoon and modern biodiversity resulted from the rise of eastern Tibet. Sci. Bull. 67, 2245–2258. https://doi.org/10.1016/j.scib.2022.10.006.

Henkes, G.A., Passey, B.H., Grossman, E.L., Shenton, B.J., Pérez-Huerta, A., Yancey, T.E., 2014. Temperature limits for preservation of primary calcite clumped isotope paleotemperatures. Geochim. Cosmochim. Acta 139, 362–382. https://doi.org/10.1016/j.gca.2014.04.040.

Hoke, G.D., Liu-Zeng, J., Hren, M.T., Wissink, G.K., Garzione, C.N., 2014. Stable isotopes reveal high southeast Tibetan Plateau margin since the Paleogene. Earth Planet. Sci. Lett. 394, 270–278. https://doi.org/10.1016/j.epsl.2014.03.007.

Hoke, G.D., 2018. Geochronology transforms our view of how Tibet's southeast margin evolved. Geology 46, 95–96. https://doi.org/10.1130/focus012018.1.

Hoorn, C., Perrigo, A., Antonelli, A., 2018. Mountains, Climate and Biodiversity. West Sussex, UK.

Horton, B.K., Yin, A., Spurlin, M.S., Zhou, J., Wang, J., 2002. Paleocene-Eocene syncontractional sedimentation in narrow, lacustrine-dominated basins of east-Central Tibet. Geol. Soc. Am. Bull. 114, 771–786. https://doi.org/10.1130/0016-7606(2002)114<0771:Pessin>2.0.Co;2.

Huang, W., Chen, F., Feng, S., Chen, J., Zhang, X., 2013. Interannual precipitation variations in the mid-latitude Asia and their association with large-scale atmospheric circulation. Chin. Sci. Bull. 58, 3962–3968. https://doi.org/10.1007/s11434-013-5970-4.

Huntington, K.W., Lechler, A.R., 2015. Carbonate clumped isotope thermometry in continental tectonics. Tectonophysics. 647–648, 1–20. https://doi.org/10.1016/j.tecto.2015.02.019.

Ibarra, D.E., Dai, J., Gao, Y., Lang, X., Duan, P., Gao, Z., Chen, J., Methner, K., Sha, L., Tong, H., Han, X., Zhu, D., Li, Y., Tang, J., Cheng, H., Chamberlain, C.P., Wang, C., 2023. High-elevation Tibetan Plateau before India-Eurasia collision recorded by triple oxygen isotopes. Nat. Geosci. 16, 810–815. https://doi.org/10.1038/s41561-023-01243-x.

Jiang, X., Cui, X., Wu, H., Xiong, G., Zhuo, J., Lu, J., Jiang, Z., 2012. The Palaeogene deserts and their implications for the origin of monsoons on the eastern margin of the Qinghai-Xizang Plateau, SW China. Sediment. Geol. Tethyan Geol. 32, 54–63 (in Chinese with English abstract).

John, C.M., Bowen, D., 2016. Community software for challenging isotope analysis: first applications of 'Easotope' to clumped isotopes. Rapid Commun. Mass Spectrom. 30, 2285–2300. https://doi.org/10.1002/rcm.7720.

Kelson, J.R., Huntington, K.W., Schauer, A.J., Saenger, C., Lechler, A.R., 2017. Toward a universal carbonate clumped isotope calibration: diverse synthesis and preparatory methods suggest a single temperature relationship. Geochim. Cosmochim. Acta 197, 104–131. https://doi.org/10.1016/j.gca.2016.10.010.

Kelson, J.R., Huntington, K.W., Breecker, D.O., Burgener, L.K., Gallagher, T.M., Hoke, G.D., Petersen, S.V., 2020. A proxy for all seasons? A synthesis of clumped isotope data from Holocene soil carbonates. Quat. Sci. Rev. 234, 106259 https://doi.org/10.1016/j.quascirev.2020.106259.

Kim, S.-T., O'Neil, J.R., 1997. Equilibrium and nonequilibrium oxygen isotope effects in synthetic carbonates. Geochim. Cosmochim. Acta 61, 3461–3475. https://doi.org/10.1016/s0016-7037(97)00169-5.

Kirshbaum, D.J., Grant, A.L.M., 2012. Invigoration of cumulus cloud fields by mesoscale ascent. Q. J. R. Meteorol. Soc. 138, 2136–2150. https://doi.org/10.1002/qj.1954.

Li, H.A., Dai, J.G., Xu, S.Y., Liu, B.R., Han, X., Wang, Y.N., Wang, C.S., 2019. The formation and expansion of the eastern Proto-Tibetan Plateau: insights from low-temperature thermochronology. J. Asian Earth Sci. 183, 103975 https://doi.org/10.1016/j.jseaes.2019.103975.

Li, L., Fan, M., Davila, N., Jesmok, G., Mitsunaga, B., Tripati, A., Orme, D., 2018. Carbonate stable and clumped isotopic evidence for late Eocene moderate to high elevation of the east-central Tibetan Plateau and its geodynamic implications. Geol. Soc. Am. Bull. 131, 831–844. https://doi.org/10.1130/b32060.1.

Li, L., Garzione, C.N., 2023. Upward and outward growth of north-Central Tibet: mechanisms that build high-elevation, low-relief plateaus. Sci. Adv. 9, eadh3058. https://doi.org/10.1126/sciadv.adh3058.

Li, L., Lu, H., Garzione, C., Fan, M., 2022. Cenozoic paleoelevation history of the Lunpola Basin in Central Tibet: new evidence from volcanic glass hydrogen isotopes and a critical review. Earth Sci. Rev. 231, 104068 https://doi.org/10.1016/j.earscirev.2022.104068.

Licht, A., van Cappelle, M., Abels, H.A., Ladant, J.B., Trabucho-Alexandre, J., France-Lanord, C., Donnadieu, Y., Vandenberghe, J., Rigaudier, T., Lécuyer, C., Terry Jr., D., Adriaens, R., Boura, A., Guo, Z., Soe, A.N., Quade, J., Dupont-Nivet, G., Jaeger, J.J., 2014. Asian monsoons in a late Eocene greenhouse world. Nature 513, 501–506. https://doi.org/10.1038/nature13704.

Liu, J., Milne, R.I., Zhu, G.-F., Spicer, R.A., Wambulwa, M.C., Wu, Z.-Y., Boufford, D.E., Luo, Y.-H., Provan, J., Yi, T.-S., Cai, J., Wang, H., Gao, L.-M., Li, D., 2022. Name and scale matter: clarifying the geography of Tibetan Plateau and adjacent mountain regions. Glob. Planet. Chang. 215, 1–15. https://doi.org/10.1016/j.gloplacha.2022.103893.

Liu-Zeng, J., Tapponnier, P., Gaudemer, Y., Ding, L., 2008. Quantifying landscape differences across the Tibetan plateau: implications for topographic relief evolution. Case Rep. Med. 113, F04018. https://doi.org/10.1029/2007jf000897.

Ludwig, K., 2003. User's Manual for Isoplot 3.00, a Geochronological Toolkit for Microsoft Excel. Berkeley Geochronology Center Special Publication, Berkeley, California.

Meckler, A.N., Sexton, P.F., Piasecki, A.M., Leutert, T.J., Marquardt, J., Ziegler, M., Agterhuis, T., Lourens, L.J., Rae, J.W.B., Barnet, J., Tripati, A., Bernasconi, S.M., 2022. Cenozoic evolution of deep ocean temperature from clumped isotope thermometry. Science 377, 86–90. https://doi.org/10.1126/science.abk0604.

Meinicke, N., Reimi, M.A., Ravelo, A.C., Meckler, A.N., 2021. Coupled Mg/Ca and clumped isotope measurements indicate lack of substantial mixed layer cooling in the Western Pacific Warm Pool during the last 5 million years. Paleoceanogr. Paleoclimatol. 6 https://doi.org/10.1029/2020PA004115 e2020PA004115.

Molnar, P., England, P., Martinod, J., 1993. Mantle dynamics, uplift of the Tibetan Plateau, and the Indian monsoon. Rev. Geophys. 31, 357–396. https://doi.org/10.1029/93RG02030.

Molnar, P., Boos, W.R., Battisti, D.S., 2010. Orographic controls on climate and paleoclimate of Asia: thermal and mechanical roles for the Tibetan Plateau. Annu. Rev. Earth Planet. Sci. 38, 77–102. https://doi.org/10.1146/annurev-earth-040809-152456.

Mulch, A., Chamberlain, C.P., 2006. The rise and growth of Tibet. Nature 439, 670–671. https://doi.org/10.1038/439670a.

Nie, J., Ruetenik, G., Gallagher, K., Hoke, G., Garzione, C.N., Wang, W., Stockli, D., Hu, X., Wang, Z., Wang, Y., Stevens, T., Danišík, M., Liu, S., 2018. Rapid incision of the Mekong River in the middle Miocene linked to monsoonal precipitation. Nat. Geosci. 11, 944–948. https://doi.org/10.1038/s41561-018-0244-z.

Petersen, S.V., Defliese, W.F., Saenger, C., Daëron, M., Huntington, K.W., John, C.M., Kelson, J.R., Bernasconi, S.M., Colman, A.S., Kluge, T., Olack, G.A., Schauer, A.J., Bajnai, D., Bonifacie, M., Breitenbach, S.F.M., Fiebig, J., Fernandez, A.B., Henkes, G.A., Hodell, D., Katz, A., Kele, S., Lohmann, K.C., Passey, B.H., Peral, M.Y., Petrizzo, D.A., Rosenheim, B.E., Tripati, A., Venturelli, R., Young, E.D.,

Winkelstern, I.Z., 2019. Effects of improved ^{17}O correction on interlaboratory agreement in clumped isotope calibrations, estimates of mineral-specific offsets, and temperature dependence of acid digestion fractionation. Geochem. Geophys. Geosyst. 20, 3495–3519. https://doi.org/10.1029/2018GC008127.

Quade, J., Eiler, J., Daëron, M., Achyuthan, H., 2013. The clumped isotope geothermometer in soil and paleosol carbonate. Geochim. Cosmochim. Acta 105, 92–107. https://doi.org/10.1016/j.gca.2012.11.031.

Ramstein, G., Fluteau, F., Besse, J., Joussaume, S., 1997. Effect of orogeny, plate motion and land-sea distribution on Eurasian climate change over the past 30 million years. Nature 386, 788–795. https://doi.org/10.1038/386788a0.

Rosenbaum, J., Sheppard, S.M.F., 1986. An isotopic study of siderites, dolomites and ankerites at high temperatures. Geochim. Cosmochim. Acta 50, 1147–1150. https://doi.org/10.1016/0016-7037(86)90396-0.

Rowley, D.B., 2007. Stable isotope-based paleoaltimetry: theory and validation. Rev. Mineral. Geochem. 66, 23–52. https://doi.org/10.2138/rmg.2007.66.2.

Royden, L.H., Burchfiel, B.C., King, R.W., Wang, E., Chen, Z.L., Shen, F., Liu, Y.P., 1997. Surface deformation and lower crustal flow in eastern Tibet. Science 276, 788–790. https://doi.org/10.1126/science.276.5313.788.

Sarr, A.-C., Donnadieu, Y., Bolton, C.T., Ladant, J.-B., Licht, A., Fluteau, F., Laugié, M., Tardif, D., Dupont-Nivet, G., 2022. Neogene South Asian monsoon rainfall and wind histories diverged due to topographic effects. Nat. Geosci. 15, 314–319. https://doi.org/10.1038/s41561-022-00919-0.

Sláma, J., Košler, J., Condon, D.J., Crowley, J.L., Gerdes, A., Hanchar, J.M., Horstwood, M.S., Morris, G.A., Nasdala, L., Norberg, N., 2008. Plešovice zircon−a new natural reference material for U−Pb and Hf isotopic microanalysis. Chem. Geol. 249, 1–35. https://doi.org/10.1016/j.chemgeo.2007.11.005.

Spicer, R.A., Yang, J., Herman, A., Kodrul, T., Aleksandrova, G., Maslova, N., Spicer, T., Ding, L., Xu, Q., Shukla, A., Srivastava, G., Mehrotra, R., Liu, X.-Y., Jin, J.-H., 2017. Paleogene monsoons across India and South China: drivers of biotic change. Gondwana Res. 49, 350–363. https://doi.org/10.1016/j.gr.2017.06.006.

Spicer, R.A., Su, T., Valdes, P.J., Farnsworth, A., Wu, F.-X., Shi, G., Spicer, T.E.V., Zhou, Z., 2021. Why 'the uplift of the Tibetan Plateau' is a myth. Natl. Sci. Rev. 8 https://doi.org/10.1093/nsr/nwaa091 nwaa091.

Spurlin, M.S., Yin, A., Horton, B.K., Zhou, J., Wang, J., 2005. Structural evolution of the Yushu-Nangqian region and its relationship to syncollisional igneous activity, east-Central Tibet. Geol. Soc. Am. Bull. 117, 1293–1317. https://doi.org/10.1130/b25572.1.

Su, T., Spicer, R.A., Li, S.-H., Xu, H., Huang, J., Sherlock, S., Huang, Y.-J., Li, S.-F., Wang, L., Jia, L.-B., Deng, W.-Y.-D., Liu, J., Deng, C.-L., Zhang, S.-T., Valdes, P.J., Zhou, Z.-K., 2019. Uplift, climate and biotic changes at the Eocene−Oligocene transition in South-Eastern Tibet. Natl. Sci. Rev. 6, 495–504. https://doi.org/10.1093/nsr/nwy062.

Su, T., Spicer, R.A., Wu, F.-X., Farnsworth, A., Huang, J., Del Rio, C., Deng, T., Ding, L., Deng, W.-Y.-D., Huang, Y.-J., Hughes, A., Jia, L.-B., Jin, J.-H., Li, S.-F., Liang, S.-Q., Liu, J., Liu, X.-Y., Sherlock, S., Spicer, T., Srivastava, G., Srivastava, G., Tang, H., Valdes, P., Wang, T.-X., Widdowson, M., Xing, Y.-W., Xu, C.-L., Yang, J., Zhang, C., Zhang, S.-T., Zhang, X.-W., Zhao, F., Zhou, Z.-K., 2020. A Middle Eocene lowland humid subtropical "Shangri-La" ecosystem in Central Tibet. Proc. Natl. Acad. Sci. U. S. A. 117, 32989–32995. https://doi.org/10.1073/pnas.2012647117.

Sun, H., Li, Z.-M., 2003. Qinghai-Tibetan Plateau uplift and its impacts on Tethys flora. Adv. Earth Science 18, 852–862 (in Chinese with English abstract).

Sun, J., Zhang, Z., Cao, M., Windley, B.F., Tian, S., Sha, J., Abdulov, S., Gadoev, M., Oimahmadov, I., 2020. Timing of seawater retreat from proto-Paratethys, sedimentary provenance, and tectonic rotations in the late Eocene−early Oligocene in the Tajik Basin, Central Asia. Palaeogeogr. Palaeoclimatol. Palaeoecol. 545, 1–15. https://doi.org/10.1016/j.palaeo.2020.109657.

Tao, J.-R., Du, N.-Q., 1987. Miocene flora from Markam country and fossil records of Betualceae. Acta Bot. Sin. 29, 649–655 (in Chinese with English abstract).

Tao, Y., Zhang, H., Zhang, J., Pang, J., Wang, Y., Wu, Y., Zhao, X., Huang, F., Ma, Z., 2022. Late Cretaceous–Early Cenozoic exhumation across the Yalong thrust belt in eastern Tibet and its implications for outward plateau growth. Glob. Planet. Chang. 216, 1–10. https://doi.org/10.1016/j.gloplacha.2022.103897.

Tardif, D., Fluteau, F., Donnadieu, Y., Le Hir, G., Ladant, J.-B., Sepulchre, P., Licht, A., Poblete, F., Dupont-Nivet, G., 2020. The origin of Asian monsoons: a modelling perspective. Clim. Past 16, 847–865. https://doi.org/10.5194/cp-16-847-2020.

Thomson, J.R., Holden, P.B., Anand, P., Edwards, N.R., Porchier, C.A., Harris, N.B.W., 2021. Tectonic and climatic drivers of Asian monsoon evolution. Nat. Commun. 12, 4022. https://doi.org/10.1038/s41467-021-24244-z.

Tian, J., Spicer, R.A., Huang, J., Zhou, Z., Su, T., Widdowson, M., Jia, L., Li, S., Wu, W., Xue, L., Luo, P., Zhang, S., 2021. New early Oligocene zircon U−Pb dates for the 'Miocene' Wenshan Basin, Yunnan, China: biodiversity and paleoenvironment. Earth Planet. Sci. Lett. 565, 116929 https://doi.org/10.1016/j.epsl.2021.116929.

Tong, Y., Yang, Z., Mao, C., Pei, J., Pu, Z., Xu, Y., 2017. Paleomagnetism of Eocene red-beds in the eastern part of the Qiangtang Terrane and its implications for uplift and

southward crustal extrusion in the southeastern edge of the Tibetan Plateau. Earth Planet. Sci. Lett. 475, 1–14. https://doi.org/10.1016/j.epsl.2017.07.026.

Wang, E., Burchfiel, B.C., Royden, L.H., Chen, L., Chen, J., Li, W., Chen, Z., 1998. Late Cenozoic Xianshuihe-Xiaojiang, Red River, and Dali Fault Systems of Southwestern Sichuan and Central Yunnan, China. Geol. Soc. Am. Bull, Colorado, USA.

Wang, C., Dai, J., Zhao, X., Li, Y., Graham, S.A., He, D., Ran, B., Meng, J., 2014. Outward-growth of the Tibetan Plateau during the Cenozoic: a review. Tectonophysics 621, 1–43. https://doi.org/10.1016/j.tecto.2014.01.036.

Wang, W., Liu-Zeng, J., Zeng, L., Wang, W., Tang, M., Zhang, J., 2022. Crustal thickness and paleo-elevation in SE Tibet during the Eocene–Oligocene: insights from whole-rock La/Yb ratios. Tectonophysics 839, 229523. https://doi.org/10.1016/j.tecto.2022.229523.

Wang, T., He, S., Zhang, Q., Ding, L., Farnsworth, A., Cai, F., Wang, C., Xie, J., Li, G., Sheng, J., Yue, Y., 2023. Ice sheet expansion in the Cretaceous greenhouse world. Fundam. Res. https://doi.org/10.1016/j.fmre.2023.05.005.

Wei, Y., He, R., Yuan, X., Li, W., Ji, Z., Niu, X., Li, Z., 2022. Lateral growth mechanism of proto-Tibetan Plateau in the late Paleogene: implications from detailed crustal structures of the Hoh Xil Basin. Geophys. Res. Lett. 49 https://doi.org/10.1029/2022gl097983 e2022GL097983.

Westerhold, T., Marwan, N., Drury, A.J., Liebrand, D., Agnini, C., Anagnostou, E., Barnet, J.S.K., Bohaty, S.M., De Vleeschouwer, D., Florindo, F., Frederichs, T., Hodell, D.A., Holbourn, A.E., Kroon, D., Lauretano, V., Littler, K., Lourens, L.J., Lyle, M., Pälike, H., Röhl, U., Tian, J., Wilkens, R.H., Wilson, P.A., Zachos, J.C., 2020. An astronomically dated record of Earth's climate and its predictability over the last 66 million years. Science 369, 1383–1387. https://doi.org/10.1126/science.aba6853.

Wiedenbeck, M., Alle, P., Corfu, F., Griffin, W.L., Meier, M., Oberli, F., von Quadt, A., Roddick, J.C., Speigel, W., 1995. Natural zircon standards for U–Th–Pb, Lu–Hf, trace-element and REE analyses. Geostand. Newslett. 19, 1–23. https://doi.org/10.1111/j.1751-908X.1995.tb00147.x.

Wu, J., Zhang, K., Xu, Y., Wang, G., Garzione, C.N., Eiler, J., Leloup, P.H., Sorrel, P., Mahéo, G., 2018. Paleoelevations in the Jianchuan Basin of the southeastern Tibetan Plateau based on stable isotope and pollen grain analyses. Palaeogeogr. Palaeoclimatol. Palaeoecol. 510, 93–108. https://doi.org/10.1016/j.palaeo.2018.03.030.

Xiong, Z., Ding, L., Spicer, R.A., Farnsworth, A., Wang, X., Valdes, P.J., Su, T., Zhang, Q., Zhang, L., Cai, F., Wang, H., Li, Z., Song, P., Guo, X., Yue, Y., 2020. The early Eocene rise of the Gonjo Basin, SE Tibet: from low desert to high forest. Earth Planet. Sci. Lett. 543, 116312 https://doi.org/10.1016/j.epsl.2020.116312.

Xiong, Z., Liu, X., Ding, L., Farnsworth, A., Spicer, R.A., Xu, Q., Valdes, P., He, S., Zeng, D., Wang, C., Li, Z., Guo, X., Su, T., Zhao, C., Wang, H., Yue, Y., 2022. The rise and demise of the Paleogene Central Tibetan Valley. Sci. Adv. 8, eabj0944. https://doi.org/10.1126/sciadv.abj0944.

Xu, Q., Ding, L., Zhang, L., Cai, F., Lai, Q., Yang, D., Liu-Zeng, J., 2013. Paleogene high elevations in the Qiangtang Terrane, central Tibetan Plateau. Earth Planet. Sci. Lett. 362, 31–42. https://doi.org/10.1016/j.epsl.2012.11.058.

Xu, Q., Ding, L., Cao, Y., Cai, F., Li, S., Tan, X., Kershaw, S., Tang, H., 2022. Late cretaceous−early Paleogene rise of the Gangdese magmatic arc (South Tibet) from sea level to high mountains. Geol. Soc. Am. Bull. 135 (7–8), 1939–1954. https://doi.org/10.1130/b36438.1.

Yang, R., Fellin, M.G., Herman, F., Willett, S.D., Wang, W., Maden, C., 2016. Spatial and temporal pattern of erosion in the three Rivers Region, southeastern Tibet. Earth Planet. Sci. Lett. 433, 10–20. https://doi.org/10.1016/j.epsl.2015.10.032.

Yao, T., Wu, F., Ding, L., Sun, J., Zhu, L., Piao, S., Deng, T., Ni, X., Zheng, H., Ouyang, H., 2015. Multispherical interactions and their effects on the Tibetan Plateau's earth system: a review of the recent researches. Natl. Sci. Rev. 2, 468–488. https://doi.org/10.1093/nsr/nwv070.

Yin, A., Harrison, T.M., 2000. Geologic evolution of the Himalayan-Tibetan orogen. Annu. Rev. Earth Planet. Sci. 28, 211–280. https://doi.org/10.1146/annurev.earth.28.1.211.

Zhang, H., He, W., Wang, J., Xie, G., 2005. $^{40}Ar/^{39}Ar$ chronology and geochemistry of high-K volcanic rocks in the Mangkang basin,Tibet. Sci. China Ser. D Earth Sci. 48, 1–12. https://doi.org/10.1360/03yd0125.

Zheng, H., Yang, Q., Cao, S., Clift, P.D., He, M., Kano, A., Sakuma, A., Xu, H., Tada, R., Jourdan, F., 2022. From desert to monsoon: irreversible climatic transition at ~36 Ma in southeastern Tibetan Plateau. Prog Earth Planet Sci 9, 1–14. https://doi.org/10.1186/s40645-022-00470-x.

Zhou, Z., Liu, J., Chen, L., Spicer, R., Li, S., Huang, J., Zhang, S., Huang, Y., Jia, L., Hu, J., Su, T., 2023. Cenozoic plants from Tibet: an extraordinary decade of discovery, understanding and implications. Sci. China Earth Sci. 66, 205–226. https://doi.org/10.1007/s11430-022-9980-9.

Zhu, C., Meng, J., Hu, Y., Wang, C., Zhang, J., 2019. East-Central Asian climate evolved with the northward migration of the high proto-Tibetan Plateau. Geophys. Res. Lett. 46, 8397–8406. https://doi.org/10.1029/2019gl082703.